Changes of the diffusion parameters of brain tissue caused by pathologic processes- the use of diffusion tensor imaging

Dissertation

by Amir Zolal

Neurosurgery department, J.E. Purkynje University and Masaryk hospital

Usti nad Labem

Charles University in Prague

2nd Faculty of Medicine

1 Table of contents

2 Introduction 6

3 Objectives 9

4 Distant diffusion changes in the pyramidal tract caused by tumor growth 10

4.1 Introduction 10

4.2 Materials and methods 11

4.2.1 Patients 11

4.2.2 MRI acquisition and DTI fiber tracking and analysis 15

4.2.3 Statistical analysis 18

4.3 Results 19

4.3.1 Fractional anisotropy 19

4.3.2 Trace 19

4.3.3 Linear, planar and spherical indices 20

4.3.4 Eigenvalues 20

4.3.5 Diagonal components of the diffusion tensor matrix 21

4.3.6 B0 intensity 21

4.3.7 FA and trace in symptomatic and asymptomatic patients 21

4.4 Discussion 23

4.5 Conclusion 27

5 The effect of a gadolinium-based contrast agent on diffusion tensor imaging 28

5.1 Introduction 28

5.2 Materials and methods 29

5.2.1 Patients 29

5.2.2 Acquisition of the images 29

5.2.3 Image processing and analysis 30

5.2.4 Statistical analysis 32
5.3 Results 33
5.3.1 Fractional anisotropy 33
5.3.2 Spherical, planar and linear indices 33
5.3.3 Components of the diffusion tensor matrix 34
5.3.4 Trace 35
5.3.5 Eigenvalues 36
5.4 Discussion 37
5.5 Conclusion 42
6 Comparison of the DTI reconstructions of the pyramidal tract with Ojemann subcortical stimulation 43
6.1 Introduction 43
6.1.1 Methods 45
6.1.2 DTI acquisition and analysis, volumetric assessment of the resection 52
6.1.3 Comparison with direct electrical subcortical stimulation 55
6.2 Results 58
6.2.1 Comparison of the tract-tumor distances with the results of the subcortical stimulation 58
6.2.2 Extent of the resection 65
6.2.3 Short-term clinical outcome 66
6.3 Discussion 68
6.4 Conclusion 74
6.5 74
6.6 75
7 Anatomy and somatotopy of the pyramidal tract in its supraventricular portion 75
7.1 Introduction 75

7.2 Methods 76
7.2.1 Patients 76
7.2.2 DTI acquisition and analysis, comparison with subcortical stimulation 78
7.2.3 DTI study of the somatotopy of the supraventricular corticospinal fibers 79
7.2.4 Anatomical dissections 81
7.3 Results 82
7.3.1 Influence of the position of the stimulation site on the extremity responding to subcortical stimulation 82
7.3.2 Location of arm and leg fibers on DTT reconstructions 82
7.3.3 Anatomical dissections 83
7.4 Discussion 87
7.5 Conclusion 90
8 The use of diffusion tensor imaging to investigate the aberant anatomy of the long descending tracts in Chiari III malformation 91
8.1 Introduction 91
8.2 Case Report 91
8.3 Discussion 95
8.4 Conclusion 97
9 Conclusions 98
10 References 100
11 List of author's publications 109
11.1 Publications on the topic of the dissertation (with impact factor) 109
11.2 Other publications with impact factor 110

2 Introduction

In 1965, the chemicist Edward O. Stejskal and his doctoral student John E. Tanner described the possibility of measurement of the diffusion of water molecules with the use of the nuclear magnetic resonance and magnetic field gradient systems [1]. However, it was not until the 1970s that the magnetic resonance started to be used for imaging, and not until the 1990s that the diffusion weighted imaging was used in medical research to detect the preferential direction of the diffusion using a mathematical model called "tensor" [2; 3], leading to the coining of the term diffusion tensor imaging (DTI). The first uses in depicting white matter tracts came just before the break of the century in 1999 [4], and the first few studies describing the use in brain tumor patients relied on manual segmentation of the tracts from colored maps [5; 6]. In 2005, Nimsky et al. published the first larger series, where the depiction of the pyramidal tract was aided by an automated tracking technique [7; 8]. Since then, neurosurgery and the neurosciences in general have seen a fast rise of interest in the technique, with many publications regarding DTI being published each year.

To simplify the description in a great deal, the technique relies on the detection of signal loss caused by the random motion of water molecules. From voxel intensities reflecting the amount of this signal loss, the diffusion constants are estimated. This information is then used to reconstruct the diffusion tensor, which represents a mathematical model of the strength of the diffusion in each voxel, thus creating a three-dimensional map of diffusion strengths and directions in the whole imaged volume. This map can be viewed; color is typically used to code the direction, intensity to code the strength of the diffusion. To depict a single tract within the whole white matter volume, automated tracking techniques such as FACT (fiber assignment by continuous tracking) or TEND (tensor deflection) with various thresholding parameters are used.

Apart from the use of the DTI for the anatomical depiction (which has also been aptly called in-vivo dissection by some authors [9]) of various tracts, the data obtained in the diffusion tensor map can be used to investigate the integrity of the white matter in

various pathologic processes or the differences in white matter structure in relation to various functional abilities of individuals [10].

I have decided to include both anatomical studies and studies concerning the changes of diffusion indices in this doctoral thesis. As to the changes in the white matter induced by the presence of tumors, various studies have described the changes of the diffusion indices in the peritumoral edema or in the normal-appearing white matter (NAWM) adjacent to tumors [11–14], however, few have described the changes occurring as a result of tumor expansion in a relatively distant, anatomically defined area [15]. The fourth chapter of this thesis describes the diffusion changes observed in the brainstem, in patients with a supraventricular glioblastoma or metastasis. The fifth chapter describes how the measurements of the diffusion indices are influenced by the presence of a paramagnetic gadolinium-based contrast agent. This is an interesting technical aspect of the technique, moreover, there have only been two studies published regarding this subject [16; 17] previous to the publication of our results [18].

The sixth, seventh and eighth chapter describe the use of the DTI fiber tracing technique to depict the normal or abnormal anatomy of the white matter. The sixth chapter describes the verification of the accuracy of the DTI depiction of the pyramidal tract by comparison with direct subcortical stimulation. Various studies have been published on this topic, most of them confirming the anatomical accuracy of the DTI-derived models of the pyramidal tract [19–21]. The seventh chapter describes both “in vivo” and actual dissections of the supraventricular portion of the pyramidal tract. The eighth chapter represents a published case description illustrating how the technique can be useful in the determination of white matter anatomy even in congenital malformations.

As the doctoral thesis consists of five separate studies, and as the topics included in the thesis are rather different from each other, different settings of statistical significance was used in each of the chapters. The conclusions are contained at the end of each chapter and summarized again at the end of the thesis, where they are given in a form of a list corresponding to the list of the objectives defined at the beginning of the thesis. The numbering of the tables and figures is separate for the chapters. On the other hand,

references have been added at the end of this thesis and the numbering is common for all chapters.

3 Objectives

1. To evaluate the changes induced by the presence of a malignant brain tumor on the white matter tracts by analyzing the diffusion parameters in regions distant to the tumor or the peritumoral edema.

2. To assess the changes in the measured diffusion indices caused by the presence of a gadolinium-based contrast agent.

3. To assess the congruence of the DTI-derived models of the pyramidal tract with direct subcortical electrostimulation in order to verify the anatomical accuracy of these models. To establish logistic regression models using our data and infer the probability of a. positive subcortical stimulation (eliciting a motor response) b. transient postoperative deterioration and c. non-radical resection, in relationship to the tumor-pyramidal tract distance.

4. To investigate the somatotopy and anatomy of the pyramidal tract in its supraventricular course using DTI and anatomical dissections.

5. To assess the utility of the technique for depicting the course of the large descending tracts in Chiari III malformation.

4 Distant diffusion changes in the pyramidal tract caused by tumor growth

4.1 Introduction

Diffusion tensor imaging (DTI) allows for noninvasive measurement of diffusion indices that can be used to evaluate the integrity of the white matter of the human brain. This technique can be used in both pathological and physiologic conditions, with applications over a range of research topics including the correlation of focal white matter indices with cognitive abilities, the investigation of white matter anatomy, the evaluation of white matter compromise in degenerative and demyelinating diseases and for many other purposes. From the neurosurgical perspective, apart from the depiction of normal white matter anatomy in vivo, the greatest interest has been focused on the depiction of altered tract anatomy in intraaxial tumors.

The changes in white matter diffusion indices caused by intraaxial tumors have been evaluated by various authors [12; 14; 22]. In principle, the tract affected by the tumor growth can be affected by the peritumoral edema, infiltrated, disrupted or dislocated [23]. The existing literature generally consists of ROI- (region of interest) based studies that evaluated the diffusion indices in the tumor tissue, the peritumoral edema and the peritumoral normal appearing white matter. In general, in the vicinity of intraaxial tumors, the FA values have been shown to be decreased and the MD values increased even in the normal appearing white matter (NAWM) adjacent to the peritumoral T2 hyperintensity, suggesting that the compromise of the white matter is not limited to the space identified as tumor mass or peritumoral edema on conventional imaging. Various studies have also examined the MRI changes caused by the Wallerian degeneration of white matter tracts caused by tumors [13; 15; 24–26] and various other lesions [27–29]. Although the majority of the studies focusing on tumor changes included only glial tumors and assumed that the observed changes arise from anatomical disruption of the tract, there may be different mechanisms causing the changes in space-occupying lesions, such as gliomas and cerebral metastases. We have decided to investigate the diffusion changes reflecting the compromise of the pyramidal tract in patients with

glioblastomas and metastases located near to this tract as identified on diffusion tensor imaging.

4.2 Materials and methods

4.2.1 Patients

For the purpose of this study, we have retrospectively identified 21 patients in our DTI database fulfilling the following criteria: 1. histologically proven glioblastoma or metastasis; 2. shortest distance from the enhancing portion of the tumor to the pyramidal tract less than or equal to 10 mm; 3. distance from the first selected ROI in the cerebral peduncle (see below) to the enhancing portion of the tumor of at least 15 mm; 4. distance from the first selected ROI in the cerebral peduncle to the peritumoral infiltration / edema identified as hyperintensity on B0 images of at least 10 mm. In the resulting patient group, there were 10 female and 11 male patients, age 47-82 years, average 62.4 ± SD 8.5. All patients underwent tumor resection or biopsy, and a histological diagnosis of cerebral metastasis (n=9) or glioblastoma (n=12) was established. Fifteen of the twenty one patients presented with a variable degree of hemiparesis. The data were acquired in the period of May 2008 till July 2010. An overview of the patients, clinical findings, tumor types and anatomical locations of the tumors is presented in Table 1. We have included a short summary of the clinical examination results obtained at the time of acquisition, the tumor tract distance in millimeters and an anatomical description of the tumor's location and extent.

N	Clinical findings	Tumor type* and location	Tumor-tract distance
1	head, LUE no motor paresis, no pronator drift, LLE distal 0/5, knee and hip flexion 3/5	left frontal (precentral gyrus with subcortical extension)	0
2	severe left hemiparesis LUE no active movement, LLE 1/5 proximal, 0/5 distal,	right parietal, P1 cortical and subcortical extension	7
3	generalized seizures, no motor or sensory deficit	right parietal, postcentral gyrus cortical and subcortical	4
4	LUE pronator drift 10 cm/ 30 sec, paresis LUE and LLE 4/5, able to walk with cane	right parietal, subcortical under the postcentral gyrus laterally	0
5	right hemiparesis, pronator drift 10 cm / 30 sec, proximal segments RUE 4/5, distal segments 5/5, RLE no paresis	left temporal pole, extending into the subcortical white matter dorsally and medially	6
6	left hemiparesis worse on the UE (pronator drift 20 cm / 30 seconds), all segments 4-/5, LLE no paresis, cognitive impairment (slowness)	cystic tumor, cyst extending into the right frontal, temporal and parietal lobe subcortically, enhancing portion right temporal T1 cortical	9
7	head: no paresis, LUE: mild paresis (4/5 predominantly proximal), LLE: severe paresis (4/5 proximal segments, 3/5	right parietal (P1, semioval center)	0

	distal segments), pronator drift 10cm/30sec, right side: no paresis, able to walk with aid and assistance		
8	Jackson seizures, head: no paresis, RUE: no paresis, RLE: distal 0/5, knee+hip flexion 3/5, unable to walk	left frontoparietal, 2 enhancing lestions (1. left frontal precentral, 2. left frontal postcentral)	0
9	expressive aphasia, moderate right side hemiparesis (pronator drift 10 cm / 30 seconds), right upper extremity worse (proximal 3/5, distal 4/5) than lower extremity (4+/5 all segments), able to walk without assistance	left fronto-parietal (semioval center)	3
10	severe expressive aphasia, pronator drift 20 cm / 30 seconds, RUE all segments 3/5, RLE all segments 4/5, walks with cane short distance	left fronto-parietal (semioval center)	0
11	left hemiparesis, LUE no pronator drift, muscle strength 5/5 all segments, LLE paresis 4/5, able to walk with cane or wheeled aid	right frontal F1 cortical and subcortical	3
12	no paresis, no pronator drift	right parietal - cortical in precentral operculum, extending posteriorly into	2

		the subcortical white matter	
13	right hemiparesis, RUE worse, predominantly distal paresis, cannot write or perform fine movements, all segments strength 4/5, pronator drift 10 cm/30 sec, RLE no paresis, no aphasia	lung carcinoma metastasis; left F2 direct subcortical adjacent to the precentral gyrus	2
14	presented with mild left hemiparesis and headache, no paresis apparent on admission due to pre-treatment with dexamethasone	malignant melanoma meatastasis; located in the superior and middle frontal gyri	7
15	no motor deficit, presented with disorientation	lung carcinoma metastasis; right frontal F1 and F2 cortical and subcortical	10
16	no motor deficit, presented with generalized epileptic seizure	breast carcinoma metastasis; right frontal F2 subcortical, adjacent to the precentral gyrus	2
17	left hemiparesis, LUE no pronator drift, muscle strength 5/5 all segments, LLE proximal paresis 4/5, distal no paresis	squamous cell carcinoma metastasis, no primary tumor detected; right parietal postcentral gyrus	2
18	left hemiparesis, pronator drift 10 cm / 30 sec, LUE all segments 4/5, LLE all segments 4-/5	lung carcinoma metastasis; right parietal, subcortical extension under P1 and P2	4

19	worsening right hemiparesis, RUE 2/5 elbow flexion, 1/5 all other segments, not able to test pronator drift, RLE 4/5 all segments, able to walk short distance	colorectal carcinoma metastasis; left postcentral gyrus cortical and subcortical	0
20	no hemiparesis, presented with headache and vertigo	thymic carcinoma metastasis; right F1 and F2 cortical and subcortical	6
21	mixed aphasia, no hemiparesis	small cell lung carcinoma metastasis; left P1 and P2 cortical with subcortical extension	10

Table 1. Overview of the patients. Patients 1-12 comprise the glioblastoma subgroup, patients 13 to 21 represent the metastasis subgroup. Muscle strength is indicated using the Medical Research Council grade, abbreviations: LUE, LLE and RUE, RLE – left and right upper and lower extremity respectively, F1, F2 superior and middle frontal gyri; P1, P2 superior and inferior parietal lobuli, T1, T2 superior and middle temporal gyri; *Tumor type is omitted in patients 1-12 (patients with glioblastoma)

4.2.2 MRI acquisition and DTI fiber tracking and analysis

MRI was performed using a 1.5T Symphony scanner (Siemens, Erlangen, Germany). DTI scans were acquired with the following parameters: one b=0 s/mm2 image (B0) and 6 diffusion encoding directions at b=1000 s/mm2, matrix 128x128, FOV 279x279 mm, TR/TE: 10100/96 ms (2.2x2.2x2.2 mm resolution) with two repetitions. In each case, a high resolution (1x1x1 mm resolution) sagittal or axial T1 image was acquired after intravenous gadobutrol (Gadovist, Shering, Berlin, Germany) administration in addition to the DTI for the overlay of the DTI-reconstructed fiber tracts.

Three applications were used for analysis – for preliminary measurements and inclusion into the study, the StealthViz application running on a StealthStation S7 planning station was used (Medtronic, Minneapolis, USA). The data were uploaded into the station,and

the high resolution T1 scan and the gradient scans were coregistered to the B0 image of the DTI sequence. The bilateral pyramidal tracts were reconstructed using a 3-ROI approach with the standard FACT (Fiber Assignment by Continuous Tracking) algorithm in the following manner: the starting (seeding) ROI was placed into the subcortical precentral gyrus, which was identified using anatomical landmarks on the high-resolution scan; the middle ROI was placed into the internal capsule and the end ROI into the pyramidal tract at the level of the fourth ventricle. Both the internal capsule and the pyramidal tract in the brainstem were identified on the DEC map overlaid over the high resolution T1 scan. The parameters of the fiber tracking were set as follows: high seeding density, seeding FA threshold of 0.20, stopping FA threshold of 0.10, bending angle threshold 60 degrees. Following the tracking, fibers that did not correspond to the known anatomy of the pyramidal tract (cerebellar and callosal projections, fibers not terminating in the precentral gyri, fibers extending out of the white matter, fibers crossing into the contralateral hemisphere) were manually excluded. This fiber tracking was used to measure the distance of the tumor to the tract and to select a slice of the B0 scan where the ROI placement would start. This slice was selected at the level of the carotid bifurcation and the interpenduncular cistern, the slice number was noted for further ROI markup, and the distance from the slice was measured by placing a temporary mark and measuring the distance to the enhancing portion of the tumor and the peritumoral edema. Multiplanar reconstruction with oblique views was used to identify the shortest distance. Conformance with the above-mentioned distance criteria was checked, and the data were excluded if the distances were less than 15 mm for the enhancing tumor-ROI distance (ET-ROI) or 10 mm for the peritumoral hyperintensity-ROI distance (PH-ROI).

The StealthViz application allows measurements of distances and visualizations in oblique sections, however, for detailed analysis of the diffusion indices, a specialized application, DTI studio v. 3.0.2 (https://www.mristudio.org/) was used. The data was loaded into the application and the following maps were saved in Analyze format for further analysis: the non-diffusion weighted B0, fractional anisotropy (FA), Dxx, Dyy, Dzz, and the invariants Cl, Cp, Cs, λ_1, λ_2, λ_3 and Trace. Dxx, Dyy and Dzz maps represent the diagonal components of the diffusion tensor for each voxel, the λ (lambda)

parameters represent the size of the first, second and third eigenvalue, respectively. The Cl, Cp and Cs maps represent the linear, planar and spherical indices. Trace is the sum of the three λ parameters [30]. We hereby refer the interested reader to the below-mentioned literature for a more in-depth explanation of the technical aspects of DTI, which exceeds the scope of this paper. The maps were loaded into the application ROIeditor 1.4.3 (https://www.mristudio.org/) for ROI markup and analysis. From the slice selected in StealthViz caudally, one rectangular ROI in the anatomical location of the pyramidal tract was created on each side of the cerebral peduncle (or the upper pons by extension) in five slices. The ROIs were placed symmetrically on both sides, with fixed dimensions of 4 × 4 × 1 voxels (volume 2.2 ×2.2 × 2.2 mm = 10.6 mm^3). The mean value of the above mentioned indices for each of the ROIs was saved for further analysis, resulting in a total of 105 ROI pairs (ipsilateral and contralateral to the tumor) for each index. The metastasis subgroup therefore contained data from 45 ROI pairs, the glioblastoma subgroup from 60 ROI pairs. The ROI drawing was performed on the B0 map to rule out any bias, the FA map and other indices were loaded afterwards. One investigator from the author group placed the ROIs, one senior neurosurgeon later confirmed and corrected the anatomical adequacy of the placement. The measurement and ROI markup is illustrated in Figure 1.

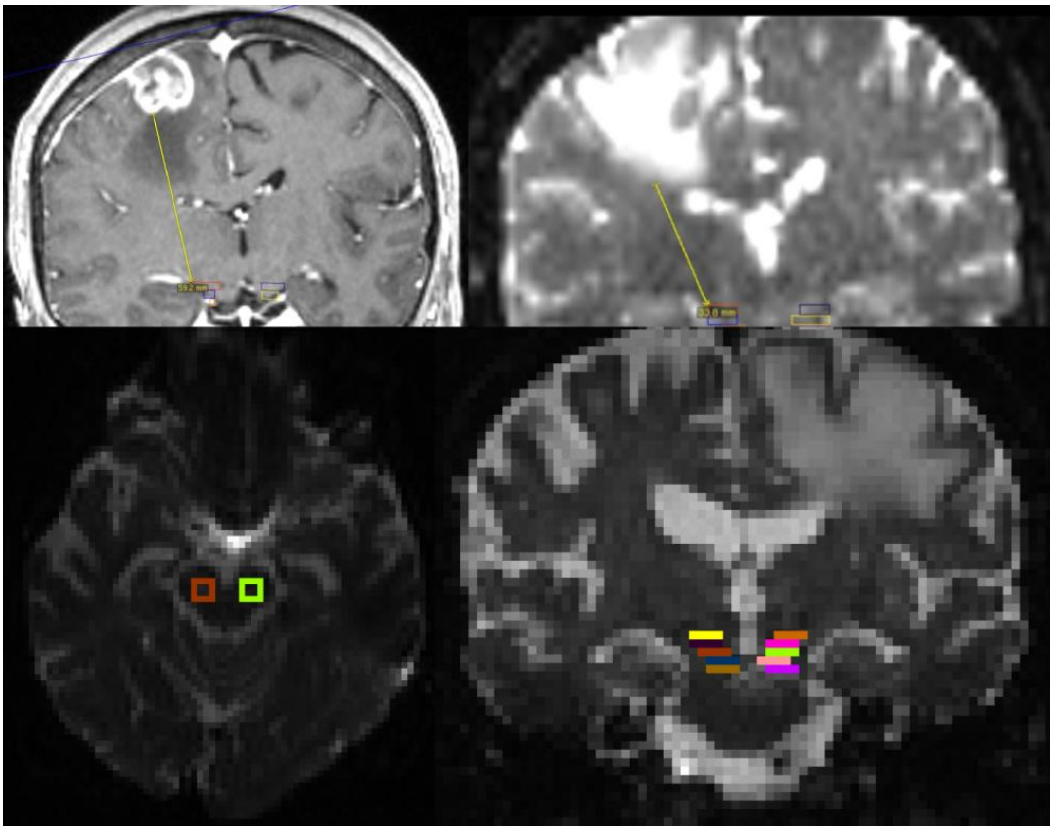

Figure 1. Above – measurement of the ET-ROI and PH-ROI distances, note the skewed appearance due to the measurement in the MPR view (StealthViz application); below – illustrations of the ROIs markup in axial and coronal plane (ROIeditor application)

4.2.3 Statistical analysis

Non-parametric methods were selected because of the greater robustness and the character of the data. The two-sided paired Wilcoxon signed-rank test was used to evaluate the differences between the mean values of the above mentioned indices obtained from the ROIs on the ipsilateral and contralateral sides to the tumor. In addition, the side-difference was calculated between the sides ipsi- and contralateral to the tumor as a subtraction of the ipsilateral from the contralateral (refered to as subtracted value index, SVI further in text). These values were compared between the metastasis and glioblastoma subgroup using the non-paired Wilcoxon rank-sum test (Mann-Whitney U test). The tests were also performed on the B0 values, to rule out any

conventional T2 hyperintensity extending into the ROIs. Additionally, the same tests were performed separately for the group of asymptomatic (no motor deficit, n=6) and symptomatic (n=15) patients for the FA and trace.

A p value of 0.01 was considered significant for all tests conducted, for simplicity, values lower than 0.001 are reported as $p<0.001$. The statistical system R, version 2.10.1 (http://www.r-project.org/) together with R commander was used for the analysis of the data.

4.3 Results

4.3.1 Fractional anisotropy

The fractional anisotropy was lower on the ipsilateral side with median difference of 0.04; this difference was statistically significant ($p < 0.001$). The fractional anisotropy was lower in both glioblastoma (median difference 0.04, $p=0.002$) and metastasis groups (median difference 0.03, $p<0.001$). The SVIs of the fractional anisotropy were not significantly different between the subgroups of glioblastoma and metastasis patients, using the non-paired Wilcoxon rank-sum test ($p=0.8$).

4.3.2 Trace

The trace value was significantly higher on the ipsilateral side for the whole group, with median difference of 7×10^{-5}, $p=0.004$. The trace value was also significantly higher on the ipsilateral side in the metastasis subgroup (median difference = 1.2×10^{-4}, $p<0.001$), but not in the glioblastoma subgroup ($p=0.5$). The difference of the SVI between the two subgroups did not reach significance ($p=0.03$, Wilcoxon rank-sum test). Boxplots of FA and trace values are shown in Figure 2.

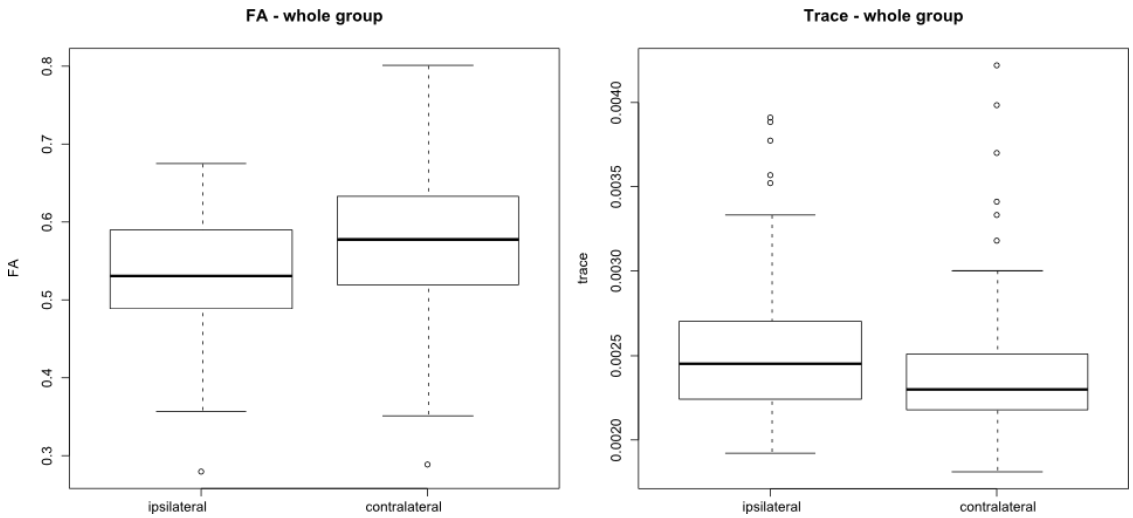

Figure 2. Boxplots of the measured FA and trace values on the sides ipsilateral and contralateral to the tumor. Outliers are represented as small circles above and below the boxplots.

4.3.3 Linear, planar and spherical indices

In the whole group, the linear index was significantly lower in the ROIs on the ipsilateral side (median difference 0.03, $p<0.001$). The same difference was observed in the metastasis and glioblastoma groups (median difference 0.03, $p=0.005$ for both groups). There was no significant difference between the ipsilateral and contralateral ROIs in the planar index ($p=0.5$) in the whole patient group or in the subgroups. Finally, the spherical index was significantly higher in the ROIs on the ipsilateral side (whole group: mean difference 0.03, $p<0.001$, metastasis group: mean difference 0.03, $p<0.001$, glioblastoma group: mean difference 0.03, $p=0.005$). There was no significant difference between the SVIs of the metastasis and glioblastoma group ($p=0.6$, Wilcoxon rank-sum test)

4.3.4 Eigenvalues

In the whole group comparison, there was a significant increase in the second and third eigenvalues ($p<0.001$), but not in the first eigenvalue ($p=0.6$). Similar results were obtained in the metastasis group, with significant second and third eigenvalue increase

($p<0.001$) and no significant difference in the first eigenvalue ($p=0.2$). In the glioblastoma group, no significant differences were found between the ipsilateral and contralateral side, although the difference in the third eigenvalue neared significance ($p=0.011$). The non-paired Wilcoxon rank-sum test was used to test for differences between the side-differences of the glioblastoma and metastasis subgroups; no significant difference was found.

4.3.5 Diagonal components of the diffusion tensor matrix

In the whole patient group, the Dxx and Dyy were significantly higher on the ipsilateral side (median difference 5×10^{-5} for both parameters, $p=0.007$ and 0.006 respectively), whereas the Dzz was not significantly different ($p=0.8$). In the metastasis group, the Dxx was also significantly higher on the ipsilateral side; no significant difference was found for the Dyy and Dzz. In the glioblastoma group, there were no significant differences between the diagonal members on the ipsi- and contralateral side. The non-paired Wilcoxon rank-sum test detected no significant differences between the SVIs of the diagonal components in the metastasis and glioblastoma subgroups on the ipsilateral or contralateral side.

4.3.6 B0 intensity

We have not found a significant difference between the B0 intensity values on the ipsilateral and contralateral side in the whole group ($p=0.6$), nor in the metastasis and glioblastoma subgroups ($p=0.1$ and 0.5 respectively) using the Wilcoxon paired test. The non-paired Wilcoxon rank-sum test showed that there was no significant difference between the SVIs of the B0 intensity values between the metastasis and glioblastoma subgroups ($p=0.7$).

4.3.7 FA and trace in symptomatic and asymptomatic patients

For the symptomatic patient subgroup, the difference between the FA values on the ipsilateral and contralateral side was highly significant (median difference 0.04, $p<0.001$), whereas for the asymptomatic subgroup, the difference was not significant, although it neared significance (median difference 0.04, $p=0.013$). There was no

significant difference between the SVIs of the symptomatic and asymptomatic patients, using the Wilcoxon rank-sum test (p=0.6).

For trace, the difference was also significant in the symptomatic patients (median difference 2×10^{-4}, p=0.002), but no significant difference in the asymptomatic patients (median difference 6×10^{-5}, p=0.9). The difference between the SVIs of the asymptomatic and symptomatic patients was not significant using the Wilcoxon rank-sum test (p=0.04).

4.4 Discussion

We have been able to show, that the presence of an aggressively growing malignant tumor near to the pyramidal tract changes the diffusion indices even in areas relatively distant to the tumor or the peritumoral edema. The FA, a measure of the structural integrity of the tract, is clearly decreased on the side ipsilateral to the tumor, suggesting that the processes causing axonal fiber degeneration are not limited to the immediate contrast enhancing area of the tumor visible on conventional MRI imaging, but may extend well into the surrounding parenchyma, either by destruction of the axons, tumor spread, or by changes in the composition and volume of the extracellular fluid. The differences of the tensor trace value (analogous to mean diffusivity) were significant in the whole group, the metastasis subgroup, but not in the glioblastoma subgroup. This fact might suggest that the mechanisms of the observed FA decrease might be different in metastases and glioblastomas, although in our series, a direct comparison using the Wilcoxon rank-sum test between the SVIs of the glioblastoma and metastasis subgroup neared, but did not reach significance. Similar difference between the glioblastoma and metastasis subgroups was evident in the eigenvalue comparison – the second (middle) and third (smallest) eigenvalues were significantly increased in the whole group, in the metastasis subgroup, but not in the glioblastoma subgroup. Although the changes in the diffusivity were also obvious in the glioblastoma subgroup (third eigenvalue increase nearing significance), we might presume that the increase in diffusivity was not absent in glioblastomas, but smaller than in metastases.

In the whole group, the linear index decreased along with the increase of the spherical index, but no change was detected in the planar index. This observation corresponded with our expectations, as the disarrangement of the axonal membranes or the increase of extracellular water content should affect the diffusivity in all directions, and not only it one plane. The analysis of the diagonal components of the diffusion tensor shows, that the increase of the diffusivity occurs preferentially in the Dxx and Dyy components, leaving the Dzz component unchanged. This is also understandable, as with disarrangement of a tract that runs almost ideally in the z-direction, we would expect the diffusivity to be relatively increased preferentially in both directions of the axial plane (x

and y). At this point, we must note that the recorded orientation of the x, y and z directions differs in various scanners and the coordinate system can be oriented along the physical orientation of the gradient fields, or recomputed to reflect the orientation of the scan. However with relatively constant head position inside of the scanner and the course of the pyramidal tract along the z-direction, we were able to observe this effect. Again, the differences were significant only for the whole group and the metastasis group only, not for the glioblastoma subgroup.

The changes observed in the whole group for FA and trace indices were also evident in the symptomatic patient subgroup. However, both the differences in FA and trace were non-significant in the asymptomatic patients. This effect was much more evident for the trace value, which is in accordance with the findings of Romano et al. [13], who observed a positive correlation between the clinical score (Bruunstrom's grading score was used in their paper) and both the FA and ADC, however, the correlation with ADC was the most significant.

There are three main factors that may play role in the occurrence of the above described changes in water diffusion in tumors. In general, the vasogenic peritumoral edema causes an extensive distention of the extracellular space in the white matter. Diffusion weighted imaging is very sensitive to these changes, and unlike conventional imaging, it can distinguish vasogenic and cytotoxic component of the edema [31]. Increased water content in the extracellular space, although undetectable without the use of statistical comparison, might therefore be one of the factors. As another possibility, some authors describing the distant changes in diffusion indices in brain tumors have presumed that the changes are caused by the Wallerian degeneration of the axons in the tract [15; 26]. Another factor, tumor infiltration might play role in the observed effects. It is known, that invasive glioma cells travel along myelinated axons and basement membranes even several centimeters from the main tumor mass [32]. It is therefore possible, that these small changes, although presumed to cause no apparent damage to the surrounding tissue, might contribute to the observed diffusion changes. To summarize, the changes induced by tumorous expansion might be well different from the changes induced by pure Wallerian degeneration seen in ischemic stroke.

Saksena et al. [15] described a decrease in FA and an increase in the MD (defined as trace / 3, thus comparable to our trace values) in corpus callosum of patients with unilateral brain glioblastoma or metastasis. Although they do not define the exact minimal distance of the tumor from the corpus callosum, they excluded all patients with midline infiltration, it is therefore safe to presume, that the studied ROIs were located in a certain distance from tumor changes visible on conventional imaging. They have concluded that the effects arise from Wallerian degeneration, rather than from tumor infiltration, because the observed effects were not different in metastases and glioblastomas in their study. The results are similar to our study regarding the character of the changes, however, there was a certain difference between the glioblastomas and metastases in our data. Another study, describing white matter changes in glioblastoma patients [13] has also shown similar diffusion changes in ROIs placed near to the tumor, but outside of any T2 abnormity. The ROIs used encompassed the pyramidal tract in the internal capsule, as confirmed by comparison with fiber tracking. In this study, the FA was shown to be decreased on the side of the tumor compared to the contralateral side; the authors used ADC (apparent diffusion coefficient) as a measure of diffusivity, which was increased on the ipsilateral side.

Some other studies describe the differences between the effects of histologically different tumors on the peritumoral white matter, useful, for instance, for differentiating metastases from high grade glial tumors [33] and meningiomas [22]. Both studies describe an increase of the mean diffusivity observed in the peritumoral T2 hyperintensity, a finding in accordance with our observation. The diffusion indices in the sections of the pyramidal tract adjacent to the tumor were evaluated by Stadelbauer et al. [12]. In only 2 of the 20 subjects with grade II-IV gliomas in their study, the volume of interest (VOI) was located inside a T2 hyperintensity. They reported a significant decrease of the FA and a significant increase of the MD compared to the contralateral side in these sections. Provenzale et al. [14] reported a significant decrease of FA in the NAWM adjacent to the T2 signal abnormity in high grade (III-IV) gliomas and no significant change of the apparent diffusion coefficient in the same ROIs. In contrast to the previous studies, Stecco et al. [34] did not find any differences in FA in the NAWM adjacent to the T2 signal hyperintensity in 17 patients examined after the resection of a

glioblastoma. An interesting study by Price et al. [35] showed that diffusion abnormities outside of the boundaries of signal abnormities on conventional T2 imaging could predict tumor recurrence. In general, the results of the above-mentioned studies support our findings of distant NAWM compromise caused by the growth of malignant tumors. However, no detailed information on the mechanisms of these changes is available at the moment.

Unlike in tumors, we might safely presume that the distant diffusion changes induced by an ischemic stroke are caused by the Wallerian degeneration. A study by Thomalla et al. [28], similarly to ours, studied the changes induced by a middle cerebral artery stroke by placing ROIs into the cerebral peduncle. The study included 9 patients, the scan was performed 2-16 days after the stroke. Their analysis included the FA, average diffusivity Dav (MD), eigenvalues and the T2 weighted signal intensity T2wSI. They have detected no difference in T2wSI, but a marked reduction of the FA on the affected side. Contrary to our findings, the Dav was not altered in their patient group. They also described a decrease in the first eigenvalue, combined with an increase in the third, with a non-significant trend towards the increase in the second eigenvalue. Another early DTI study regarding this topic [29] included five patients scanned two to six months after the stroke. The areas of the corticospinal tract distant to the area of the infarction showed decreased FA, but no changes in MD.

As the Wallerian degeneration prominent in stroke has not been shown to increase the diffusivity in the pyramidal tract, our results together with the above mentioned studies suggest, that the other two mechanisms (increased water content and tumor infiltration) may play a role in the diffusion changes caused by tumors. Our data suggest that these changes might also be dependent on the type of the tumor. However, the validity of these assumptions is limited by the relatively low numbers of patients included in both our study and the described literature.

The main weakness of our study is the small number of patients included. This is mainly caused by the strict criteria which have been applied to define tumors near to the pyramidal tract. Unlike in other studies, only patients with tumors within a distance of 10 mm or less were selected, creating a relatively homogenous group of patients.

Moreover, multiple ROI means were extracted for each of the patients, collecting enough data for a meaningful statistical comparison. The ROI definition as a uniform square object might represent another weakness of this study. We have considered using ROIs drawn manually on the FA map or portions of the previously tracked pyramidal tract, but both these techniques could introduce bias into our comparison.

Although the findings are interesting, we are not able to provide a definitive explanation of the observed diffusion changes in terms of a pathophysiological mechanism. Further studies including patients with different histological tumor entities (metastases, meningiomas) for comparison with the known findings are warranted, as well as further investigation of the changes in the white matter caused by gliomas. An interesting study would compare the distant diffusion changes in patients with brain tumors and ischemic stroke, as the results could confirm the role of Wallerian degeneration as the underlying mechanism.

4.5 Conclusion

Hemispheric glioblastomas and metastases located near to the pyramidal tract induce distant diffusion changes in the tract that are observable more than 15 mm from the tumor border, in the absence of any T2 signal changes. These changes are different in glioblastomas and metastases. Other mechanisms than the Wallerian degeneration may contribute to the observed effects.

5 The effect of a gadolinium-based contrast agent on diffusion tensor imaging

5.1 Introduction

Diffusion tensor imaging (DTI) is an MRI technique that allows the investigator to noninvasively estimate the magnitude and direction of diffusion of water molecules. When imaging the human or animal body and its tissues, this diffusion can be influenced by various factors, most notably by the presence of lipophilic membranes that causes the diffusion to be restricted in one or more directions, leading to diffusion anisotropy. The use of DTI in medicine and research has largely focused on (but not been limited to) the diffusion characteristics of the brain white matter, both under physiological conditions and also in disease. Under physiological conditions, the technique has been used to study the anatomy of white matter bundles connecting various cortical and subcortical areas, to correlate the size and quality of previously known anatomical connections among individuals with their cognitive abilities etc. In imaging brain pathology, the use of DTI in preoperative planning and intraoperative navigation might be regarded as the most important consequence of the development of diffusion tensor tracking (DTT) [36] [37].

Various technical aspects influence the results of DTT, be it the strength of the magnetic field, the strength of the gradient fields, the directions used for diffusion measurements, the experience of the operator and the algorithm used. Up to now, there have been conflicting reports about the nature of the changes of diffusion weighted and diffusion tensor imaging parameters after the administration of a gadolinium-based contrast medium, and recent studies have only covered a few of the measured diffusion parameters [16]. Therefore, no strong recommendation can be made regarding the use of gadolinium-based contrast agents prior to the acquisition of DTI data. The aim of this study was to investigate in more detail the influence of a gadolinium-based contrast agent on the measurement of water diffusion in intrinsic contrast enhancing brain tumors.

5.2 Materials and methods

5.2.1 Patients

For this study, we recruited 16 patients (5 female, 11 male, mean age 59,8 years, range 43-81), all of them harboring an intra-axial, contrast enhancing brain tumor. All patients underwent tumor resection or stereotactic biopsy following the scan, and the histological diagnosis was established. An overview of the patients, tumor locations and diagnoses is given in Table 1. All patients provided a written informed consent; the study has been approved by the local Ethics Committee.

N	Age / sex	Tumor location	Histological diagnosis
1	60 / F	right parietal	glioblastoma, WHO IV
2	55 / M	right parietooccipital	glioblastoma, WHO IV
3	68 / M	left temporoparietal	glioblastoma, WHO IV
4	43 / F	left occipital	hemangioblastoma, WHO I
5	68 / M	left temporooccipital	metastasis of pulmonary carcinoma
6	81 / F	left occipital	glioblastoma, WHO IV
7	68 / M	right parietal	glioblastoma, WHO IV
8	61 / M	left temporooccipital	glioblastoma, WHO IV
9	44 / M	right frontal	glioblastoma, WHO IV
10	65 / F	left occipital	glioblastoma, WHO IV
11	54 / M	right occipital	metastasis of pulmonary carcinoma
12	59 / F	left frontoparietal	metastasis of pulmonary carcinoma
13	47 / M	right frontal	metastasis of thymic carcinoma
14	75 / M	right frontoparietal	metastasis of urinary bladder carcinoma
15	49 / M	right parietal	metastasis of pulmonary carcinoma
16	60 / M	right frontal	glioblastoma, WHO IV

Table 1. Overview of the patient group

5.2.2 Acquisition of the images

The imaging was performed using a 1.5 T scanner (Avanto, Siemens, Erlangen, Germany). The maximum gradient strength of the scanner is 45 mT/m in the longitudinal direction and 40 mT/m in the horizontal and vertical directions. The post-contrast DTI acquisition was added to a routine preoperative examination protocol

consisting of a DTI scan and a high resolution contrast-enhanced T1 scan used for navigation. At first, a spin-echo single-shot echo-planar DTI sequence was acquired with the following parameters: one b=0 s/mm^2 image and 20 diffusion encoding directions at b=1000 s/mm^2, TR/TE 8000/94 ms, matrix 138 × 192, field of view 276 × 384 mm, isotropic voxel = 2 × 2 × 2 mm, no slice gap, number of slices = 55, acquisition time 2:45 min. After that, a fixed volume of 15 mL of Gadobutrol (Gadovist, Bayer Schering Pharma, Leverkusen, Germany) was administered and a second DTI sequence was acquired within two minutes of the application. After the second DTI scan, a high-resolution T1 sequence was acquired (TR/TE 1900/3.37, matrix 256 × 192, voxel size 1 × 1 × 1 mm).

5.2.3 Image processing and analysis

For all DTI analyses, DTI Studio v. 3.0.2 (https://www.mristudio.org/) was used. The pre-contrast DTI data were processed first, and the following maps were saved in Analyze format for further analysis: the non-diffusion weighted B0, fractional anisotropy (FA), Dxx, Dyy, Dzz, Dxy, Dxz, Dyz, and the invariants Cl, Cp, Cs, λ_1, λ_2, λ_3 and Trace. Dxx, Dyy and Dzz maps represent the diagonal components of the diffusion tensor for each voxel, whereas Dxy, Dxz and Dyz are the off-diagonal components. The λ (lambda) parameters represent the size of the first, second and third eigenvalue, respectively. The Cl, Cp and Cs maps represent the linear, planar and spherical indices. Trace is the sum of the three λ parameters [38]. We hereby refer the interested reader to the below-mentioned literature for a more in-depth explanation of the technical aspects of DTI, which exceeds the scope of this paper. In a second step, the post-contrast DTI data were processed in a similar manner. The B0 scan of the post-contrast examination was coregistered with the pre-contrast B0 using the SPM8 toolbox (Statistical Parametric Mapping 8, http://www.fil.ion.ucl.ac.uk/spm/), and the rest of the post-contrast maps were resliced in concordance with this registration. Nearest-neighbor interpolation was used to reslice the scans to avoid any artificial changes in voxel intensity. The anatomical T1 scan was also converted to Analyze format and then coregistered to the B0 scan of the pre-contrast examination. The resulting dataset after these steps were 2 sets of DTI maps (pre-contrast and post-contrast) and a spatially

coregistered anatomical T1 scan with contrast enhancement, although the high resolution of the anatomical scan was lost during the coregistration.

For ROI definition and analysis, the program ITK-SNAP [39] was used. The ROIs were drawn manually or semi-manually with the use of an “adaptive” brush with automatic intensity thresholding. The anatomical T1 scan was used for the drawing of the ROIs; 5 regions of interest in different axial slices were defined in the contrast enhancing area (CE), the peritumoral edema (PE) and both ipsilateral and contralateral normal appearing white matter (NAWM). In such manner, a total of 15 ROIs were prepared for each subject. The position of the PE and NAWM ROIs was confirmed by overlaying the resulting segmentation over the B0 scan (Figure 1). A reasonable coverage of the respective area was targeted when drawing the ROIs; due to the unequal sizes of the tumors and the peritumoral edema, no standard ROI size was chosen or attempted during the ROI selection. The resulting segmentation was saved in Analyze format and reloaded with each of the above-mentioned diffusion parameter maps; the in-built ROI statistics function of the ITK-SNAP program was used to extract and collect the average of each diffusion parameter for statistical analysis. Using this methodology, a total of 240 corresponding ROI average pairs were gained for each diffusion parameter map (5*16 = 80 for each of the above described areas). The mean ROI size in voxels for the contrast enhancing areas was 377.2 ± 237.3; for the peritumoral edema the mean ROI size was 389.8 ± 289.6 and 443.9 ± 197.3 for the NAWM.

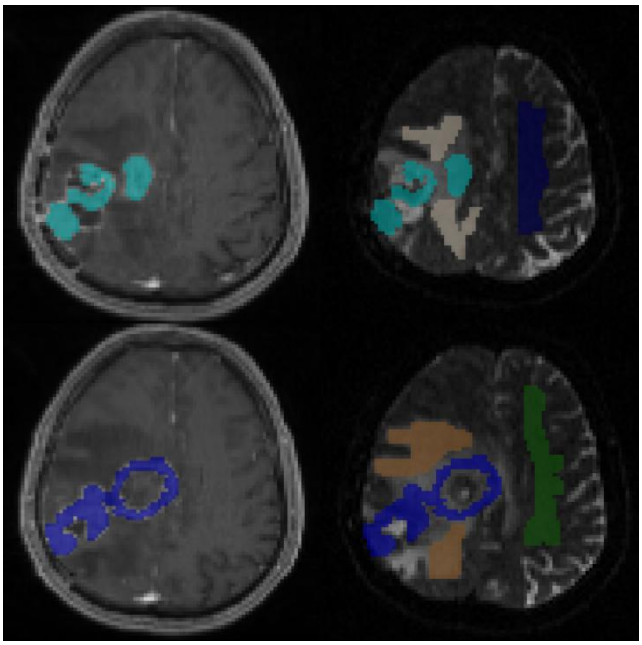

Figure 1: Patient 15, ROI definition – left – a T1 scan with gadolinium contrast, CE ROIs marked in blue color; right – PE and NAWM ROIs in the corresponding B0 slices

5.2.4 Statistical analysis

The statistical system R, version 2.10.1 (http://www.r-project.org/) together with R commander [40] was used for the analysis of the data. We decided to use non-parametric statistical tests, as our datasets consistently failed the Shapiro-Wilk test of normality. Therefore, the paired samples Wilcoxon test (two sided) was selected as the main tool for comparing the data in our datasets. For each map, a comparison was made between the pre-contrast and post-contrast averages of the corresponding ROIs. In a second step, the differences between the corresponding pre- and post-contrast ROI averages were computed (post-contrast ROI average - pre-contrast ROI average = "contrast-induced change") and compared among the above-described areas (CE, PE and NAWM) using the Mann-Whitney U test. Additionally, the Pearson correlation coefficients were computed for the pairs of pre- and post-contrast data to check for the eventual influence of the preprocessing on the data. As we used a relatively small number of samples (80 ROI averages for each region), a p-value of 0.01 or less was considered significant for

all tests. For clarity, we will specify the order of p for all tests for small numbers, or state the actual value of p further in the text.

5.3 Results

5.3.1 Fractional anisotropy

We have found a significant increase of FA in the contrast enhancing areas in the post-contrast scans, when compared to the corresponding ROI averages in the pre-contrast scans. The median increase for the contrast enhancing ROIs was 0.023 compared to the pre-contrast scans, with a p-value on the order of 1e-11. Moreover, we have found a rather small, yet significant difference between the pre- and post-contrast averages in the corresponding ROIs in the peritumoral edema (median difference = 0.005; $p \approx 1e\text{-}4$). The difference for the NAWM ROIs was just marginally insignificant (median difference = 0.005; $p > 0.01$). Using the Mann-Whitney U test, we have also compared the contrast-induced changes among the three areas we investigated and found a highly significant difference between the changes observed in the CE and PE areas ($p \approx 1e\text{-}8$) and the CE and NAWM areas ($p \approx 1e\text{-}10$). There was no significant difference between the changes in the PE and NAWM areas ($p \approx 0.6$). Pearson's correlation coefficients between the matching pairs of averages were above 0.85 and highly significant ($p < 1e\text{-}3$) for all examined regions. The results are summarized in Table 2.

	pre-contrast median / mean	post-contrast median / mean	median of the differences / mean of the differences	p
CE	0.224 / 0.228	0.246 / 0.253	0.023 / 0.025	1e-11
PE	0.218 / 0.247	0.223 / 0.253	0.005 / 0.006	1e-4
NAWM	0.476 / 0.469	0.477 / 0.471	0.005 / 0.003	1e-2

Table 2. Medians and means of the 80 measurements for each region, together with the median of the differences, the mean of the differences and p for the two sided Wilcoxon signed rank test

5.3.2 Spherical, planar and linear indices

For the linear index, we have found a significant increase in the CE (median pre-contrast: 0.18, median post-contrast: 0.2, median difference: 0.02; $p \approx 1e\text{-}10$) and PE areas (median pre-contrast: 0.2, median post-contrast: 0.2, median difference: 5e-3; $p = 0.004$). There was no significant increase in the NAWM areas ($p = 0.6$). For the planar index, only the increase in the CE was statistically significant (median pre-contrast: 0.16; median post-contrast:0.18, median difference: 0.01; $p \approx 1e\text{-}11$); the Wilcoxon test was marginal ($p=0.011$) for the PE and non-significant for the NAWM. For the spherical index however, we have detected a significant decrease in all three areas. The biggest and most significant change was detected in the CE (median pre-contrast: 0.64, median post-contrast: 0.6, median difference: 0.03; $p \approx 1e\text{-}12$). For the PE, the results were as follows: median pre-contrast 0.65, median post-contrast 0.66, median difference: 7e-3, $p \approx 1e\text{-}4$; for the NAWM: median pre-contrast: 0.36, median post-contrast: 0.36, median difference: 6e-3; $p = 7e\text{-}3$.

Again, the Mann-Whitney U test showed that the contrast-change was significantly larger in the contrast enhancing ROIs than in the peritumoral edema or NAWM for all indices; however there was no significant difference between the peritumoral edema and NAWM ROIs. Additionally, the magnitude of the contrast-induced change was compared between the linear and planar indices, but no significant differences could be detected for the CE, PE or NAWM regions.

5.3.3 Components of the diffusion tensor matrix

There was a significant decrease of all diagonal components of the diffusion tensor matrix in all areas except for the Dxx in NAWM. However, the significance of the test was much smaller for PE and NAWM than for CE in all components, and could be considered marginal. As the original values were on the order of 1e-4 to 1e-3, the median differences were rather small, generally on the order of 1e-5 or less. We have found no significant change in the off-diagonal components. The results of the paired samples Wilcoxon test are summarized in Table 3.

	Dxx	Dyy	Dzz	Dxy	Dxz	Dyz
CE	-5e-5 p ≈ 1e-8	-4e-5 p ≈ 1e-8	-4e-5 p ≈ 1e-7	-2e-6 p = 0.43	-4e-7 p = 0.7	-1e-6 p = 0.8
PE	-1e-5 p = 0.009	-1e-5 p = 0.004	-2e-5 p = 0.001	-3e-6 p=0.06	-1e-6 p = 0.44	-1e-6 p = 0.2
NAWM	-6e-6 p = 0.03	-1e-5 p = 0.001	-1e-5 p = 0.001	-2e-6 p=0.94	-1e-6 p = 0.22	6e-7 p = 0.1

Table 3. Results: median difference between pre-contrast and post-contrast scan (first line in each table cell), significance of the Wilcoxon test (second line in each table cell). Significant differences are marked with a gray background.

Secondly, the contrast-induced changes in the three examined areas (CE, PE, and NAWM) were compared among each other using the Mann-Whitney U test. We have found a significant difference between the CE and PE areas as well as between the CE and NAWM areas. There were no significant differences in the contrast-induced changes between the PE and NAWM areas. The test results are summarized in Table 4.

	Dxx	Dyy	Dzz
CE-PE	-3e-5; p ≈ 1e-5	-2e-5; p ≈ 1e-4	-2e-5; p = 0.002
CE-NAWM	-3e-5; p ≈ 1e-7	-4e-5; p ≈ 1e-7	-3e-5; p ≈ 1e-6
PE-NAWM	-3e-6; p = 0.4	-4e-6; p = 0.5	1e-6; p = 0.3

Table 4. Median differences and the significance of the Mann-Whitney U test for comparisons of the contrast-induced changes in the diagonal components; the significant differences are marked with a gray background

Also for the diffusion tensor matrix components, Pearson's correlation coefficients were high (> 0.85) and significant for all corresponding ROI pairs.

5.3.4 Trace

We have found a significant decrease in the tensor trace for all 3 areas. The median values for the pre-contrast and post-contrast CE ROIs were 3.1e-3 and 2.9e-3, respectively. The median difference was 1e-4, with p ≈ 1e-8. For the PE ROIs, the results were as follows: median pre-contrast 4e-3, median post-contrast also 4e-3, median difference 5e-5 with p ≈ 1e-5. For the NAWM: median pre-contrast 2e-3, median post-contrast also 2e-3, median difference 3e-5, p ≈ 1e-6.

We have also used the Mann-Whitney U test to compare the contrast-induced changes among the three regions and found a significantly larger change in the CE area than in the PE and NAWM areas. There was no significant difference between the contrast-induced changes in the PE and NAWM areas.

5.3.5 Eigenvalues

We have found a statistically significant decrease in all three eigenvalues for all three regions (CE, PE and NAWM). Again, the median differences are on the order of 1e-5, as the size of the eigenvalues was on the order of 1e-3. The results of the statistical analysis are shown in Table 5. Again, the contrast-induced change was significantly larger in the CE than in the PE and NAWM, and there was no difference between the PE and NAWM as shown by the Mann-Whitney U test for all eigenvalues.

		λ_1	λ_2	λ_3
CE	Median difference	-3e-5	-4e-5	-5e-5
	Significance (p) ≈	1e-6	1e-8	1e-10
PE	Median difference	-1e-5	-1e-5	-2e-5
	Significance (p) ≈	1e-3	1e-6	1e-5
NAWM	Median difference	-1e-5	-8e-6	-1e-5
	Significance (p) ≈	1e-4	1e-3	1e-3

Table 5. Overview of the results of the comparisons of pre- and post-contrast scans using the Wilcoxon paired samples test

We have also used the Wilcoxon paired samples test to compare the contrast-induced changes in the three eigenvalues. For this comparison, the contrast-induced change index was computed as a percentage of the pre-contrast value (change = 100*(pre-contrast – post-contrast)/pre-contrast). For the CE regions, we have observed the largest decrease in the third eigenvalue, with a median decrease of 5.8%, followed by the second eigenvalue with a 3.3% median decrease and the first eigenvalue with a 2.5% median change. The paired samples Wilcoxon test was highly significant ($p<1e-8$) in multiple comparisons for the differences between the three change indices. In the PE regions, the observed contrast-induced changes were smaller with median percent changes of 0.7%, 1.1% and 1.6% for the first, second and third eigenvalues, respectively. The Wilcoxon

test was significant on the order of 1e-3 to 1e-4 for multiple comparisons among these indices. For the NAWM, the observed contrast-induced changes were not significantly different between the three eigenvalues.

5.4 Discussion

In our study, we have documented the changes that occur in a clinical DTI scan after the administration of a gadolinium-based contrast agent. The changes in FA were small, and only reached a magnitude that could influence the results of the diffusion-tensor tracking in the contrast-enhancing areas. The changes that occurred in the peritumoral edema and the NAWM were on the order of magnitude of 1e-3, as the FA threshold clinically used for fiber tracking in pre-surgical planning varies around 0.25-0.30 [41; 42], one can deduce that a change two orders of magnitude smaller would not cause a major difference in the results. The linear, planar and spherical indices basically describe the anisotropy in greater detail. The changes we have observed in FA were confirmed in these indices, with the significant decrease of the spherical index in all three areas representing the fact that the effects of the gadolinium contrast agent are also observable outside of the contrast enhancing areas, although on a smaller scale. Also for the diagonal components of the diffusion tensor matrix, we have observed a decrease in all diagonal components in all three areas we have examined.

Although there were different results of the statistical tests for the PE and NAWM, a statistical comparison of the changes that occurred after contrast agent injection showed no significant difference between the PE and NAWM areas for FA, the diagonal components of the diffusion tensor matrix, or the invariant indices examined. In the contrast enhancing areas however, there were changes that were both statistically significant *per se* and statistically significantly larger than those observed in the PE or NAWM.

As we conducted the study, the only previous publication on the topic was that of Bae et al.[3] showing an overall decrease. On the other hand, our data show a rather interesting finding – a significant *increase* of FA (for illustration see Figure 2). We examined the reasons for this effect further, and we were able to show that the trace of the diffusion

tensor, defined as the sum of the three eigenvalues, diminished significantly in all three areas and that the decreases in the eigenvalues were disproportional. The third (smallest) eigenvalue decreased most, while the second eigenvalue also decreased more than the first eigenvalue, resulting in an increase of the FA as the diffusion seemingly became more unidirectional.

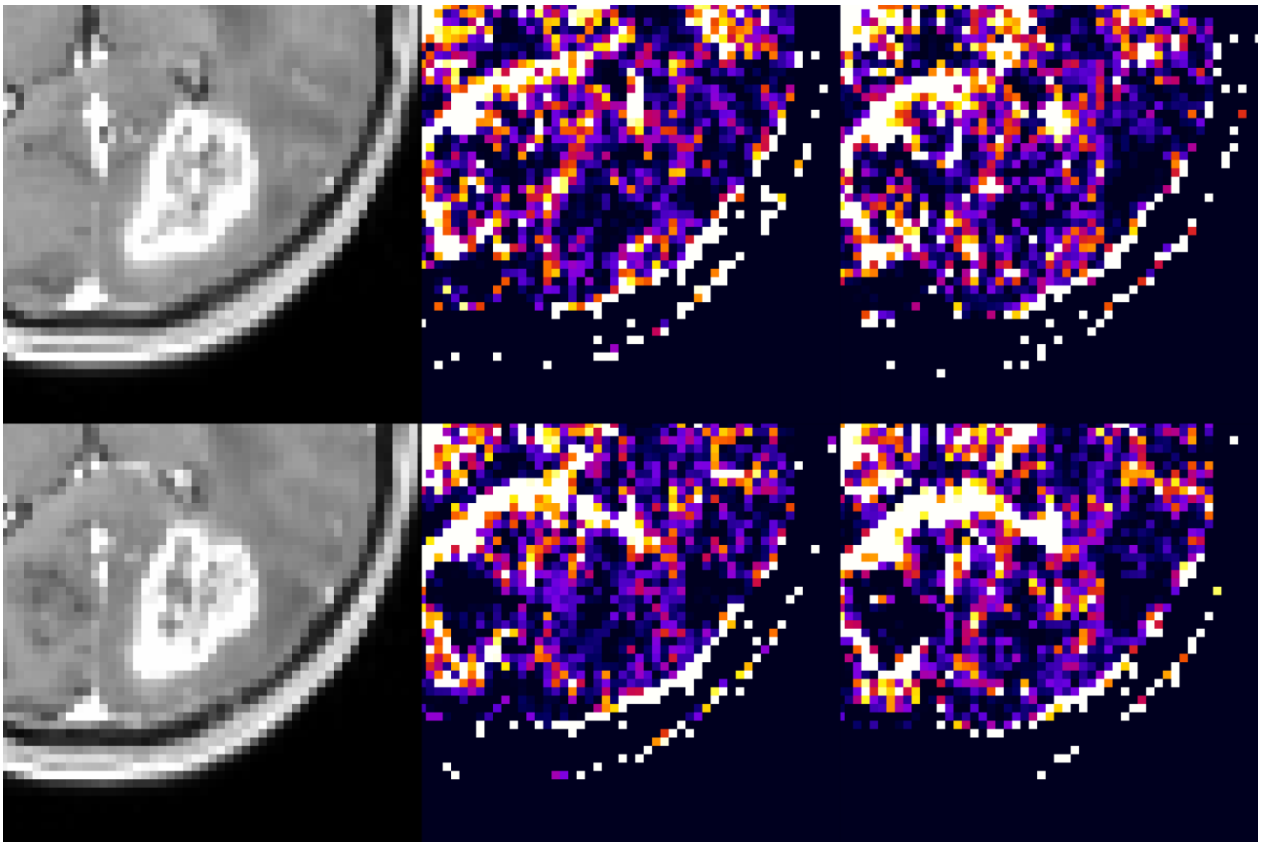

Figure 2: The increase in FA is hard to be distinguished visually on FA maps. For visualization purposes, we have enhanced the contrast of the FA maps of patient 10 by calculating the new intensity of a voxel as the original intensity cubed and divided by 16 (this was to enable the result to fit into the 16bit integer map) using ImCalc function in SPM. The resulting maps were opened in the software MRICro (www.sph.sc.edu/comd/rorden) with a color lookup table „NIH_fire"; the imaging windows were set to the same values. The figure shows two slices in a T1 scan on the left and the corresponding FA map slices with the pre-contrast slice in the middle, and the post-contrast slice on the right side. As the color lookup table displays the low intensities as black, and the color changes through blue and yellow to white in high intensities, a discreet but clearly distinguishable increase of the FA can be observed.

In contrast to the above-mentioned study [16] regarding this subject, we examined a larger number of diffusion parameters and have shown that the diffusion measurements in the NAWM might also be influenced by the contrast agent. Bae et al. used 3 large ROIs in the above-mentioned areas (CE, PE and NAWM) in 9 patients, leading to 9

mean values used for statistical analysis in each area. In these settings, the rather small effect of pre- and post-contrast DT signal differences can be obscured by gross regional variations in the diffusion characteristics (directions, eigenvalues and indices) of the tissue throughout the VOI. However, in contrast to our findings, there was an observable trend towards a decrease of the FA in all areas, yet only the change of the FA in the tumor area was significant, which is in strong contrast to our findings and also to the findings the same group reported in their more recent publication [17]. This is a larger series with a more homogenous group of subjects [17], where an *increase* of the FA has been observed, a finding that is in concordance with our results, yet only the changes in the peritumoral edema were significant. They have also observed a decrease in the first and second eigenvalues, but they did not report on the changes in the third eigenvalue. The most important observation described in this paper is that the effects of the contrast agent were only detectable for a short time (< 6 min) after administration.

Previously, there have also been contradictory results published regarding the effect of gadolinium-based contrast agents on diffusion-weighted imaging (DWI). While some have found no effect of the contrast medium on the results [43], some have reported statistically significant changes in the ADC [44]. Firat et al. [45] have also suggested that the effect on the ADC might be diminishing with time from the contrast media application. Unlike the original study of Bae et al. [16], both studies [44; 45] that have detected changes after contrast agent administration also detected statistically significant changes in normal white matter.

All of these papers described relatively large, inhomogeneous groups of patients with various pathologies. Our patient group was smaller, yet it contained only patients with intra-axial contrast enhancing tumors, and the scans were performed immediately after the administration of the contrast agent. Therefore, the effect of the contrast agent was clearly distinguishable. As we know that the type of sequence (spin-echo echo-planar) used is very sensitive to susceptibility artifacts, we would expect the paramagnetic contrast agent to have a distorting influence on the scans. As an attempt to interpret our results from a physics perspective, we suggest that the disproportionate signal attenuation in the presence of a contrast agent depends on the diffusion weighting.

Moreover, the values (as evidenced by our data) might be influenced by low-level signal clipping in the presence of background noise in a strongly T2 weighted sequence (SE-EPI with TE=94 ms). In magnitude images that are generally used in MRI, the noise in areas where the MR signal falls below noise level is rectified, thus giving rise to a non-zero „dark signal“ or „background“ artificially biasing the acquired signal, i.e. not allowing it to decay to zero. This can then lead to a decrease in the diffusion coefficient in post-contrast scans. Such a mechanism, however, is not in good accord with our current eigenvalue results, since clipping should result in a less pronounced decrease for lower eigenvalues.

In general, we have confirmed the results of previous studies that detected significant changes in measured diffusion parameters after the administration of a gadolinium contrast agent. We should stress the fact that water diffusion itself most certainly remains uninfluenced by the contrast agent and that the effects we could observe in our study are purely the result of the effect on the measurement method. Although the effects on the NAWM or PE are negligible compared to the thresholds used in DTT, it would be unwise to perform DTI scanning after contrast administration for pre-surgical planning purposes, or even more so for the examination of the diffusion parameters.

The main limitation of our study is the relatively small number of patients included. However, multiple ROI averages were extracted from each dataset, and the resulting number of measurements did not differ substantially from similar previously published studies. Other limitations include the subjective placement of the ROIs and the need to co-register the data. As mentioned above, we did not attempt to cover the respective area to the maximum extent. In order to avoid errors, we left sufficient gaps between the visible margins of the contrast enhancing and peritumoral edema. However, the resulting smaller size of the ROIs in the PE might have caused the statistical power of the analysis to be lower, resulting in the only marginal significance of some of the results compared to those in the CE and NAWM. The need to co-register the data was another limitation; although the scans were performed in one session, we would not expect the patient to lie perfectly still during the contrast agent administration. Each pair of coregistered images was carefully checked for registration errors, and none were detected in the present

study. However, partial volume effects caused by sub-voxel movements cannot be ruled out.

As we did not clarify the exact mechanism by which the contrast agent influences DTI scans, further research is warranted, although this might be regarded as a purely theoretical, rather than a clinical, matter. Ideally, this research should include experimentally adjustable MRI equipment, to study the influence of different settings on the observed effects and an even more in-depth analysis of the underlying physical interactions.

5.5 Conclusion

We have detected significant differences between the diffusion parameters in DTI scans performed before and after the administration of a gadolinium-based contrast agent. The observed effects were the strongest in the contrast enhancing areas, but some of the observed differences were also statistically significant in the peritumoral edema and the normal appearing white matter.

6 Comparison of the DTI reconstructions of the pyramidal tract with Ojemann subcortical stimulation

6.1 Introduction

The use of diffusion tensor imaging for the preoperative depiction of white matter tracts in the presence of a brain tumor was only introduced into clinical neurosurgical practice a few years ago [4], yet it has quickly attracted the interest of neurosurgeons. Since the pioneering work of Nimsky et al. [46–48] showed that the visualization of a fiber tract is not only feasible in clinical settings, but that it is also very useful both pre- and intraoperatively, there has been a range of publications describing the use of the technique to preoperatively visualize the main eloquent white matter pathways. Most efforts have concentrated on the pyramidal tract, but other publications also include the language [49; 50] and visual pathways [51; 52]. At the same time, it has been clear that the images of the tract can be difficult to reconstruct in the presence of major brain tissue edema or tumor infiltration. The commonly used fractional anisotropy (FA) thresholds must be lowered to successfully trace the tract in these circumstances, resulting in an increased presence of so-called "contaminating fibers" – fibers that do not correspond to any known anatomical tract, or fibers that even pass through CSF spaces. The reconstructed model of the tract must therefore be compared to the anatomical knowledge of the investigator and the contaminating fibers are excluded manually [20]. This high level of dependence on algorithm type, threshold setting and operator knowledge introduces a certain insecurity into the technique. Therefore, along with the interest in the technique itself, there has been a strong need to validate the results by comparison with other methods of examining the function of a particular fiber tract, either by comparing the visualization and diffusion parameters of the tract with clinical data [53], [54], or by direct electrophysiological exploration of the white matter by stimulation of the resection cavity wall.

However, there are limitations to both methods. The comparison with clinical findings tends to be crude, as pathological processes seldom involve one small particular region of white matter. The comparison with direct subcortical stimulation suffers from other

disadvantages, the major one being the inability of the surgeon to pinpoint the exact location of the stimulation point with the use of the navigation system. One of the earliest publications on this topic by Berman et al. [19] identified the mean distance between the stimulation site and the DTI reconstruction of the pyramidal tract to be 8.7 ± 3.1 mm. This included all errors encountered in the process – the error of the DTI tracking (DTT) and tract voxelization, the error of the navigation system, the brain shift and the thickness of the white matter tissue margin around the stimulation point that had to be crossed to elicit a motor response with the Ojemann stimulator. Moreover, this article described a relatively small group of 9 patients; there was no information on tumor size, patient positioning or other factors that might influence the brain shift. We can therefore assume that the actual shifting of the white matter tract can be even larger than the aforementioned average 8.7 mm in individual cases and thus the intraoperative visualization of pre-operatively reconstructed fiber tracts becomes rather unreliable for the purpose of accuracy verification. This issue is addressed by using either postoperative or even intraoperative DTI scans to determine the tract-stimulation point distance. A comparison with postoperative scans was used by Kamada et al. [55] in a reverse fashion – the DTI images of the pyramidal tract were used as a reference to evaluate the spatial thresholds of subcortical stimulation during tumor resection in various stimulation current settings. Maesawa et al. [56] used intraoperative DTT to reconstruct tracts and correlate them with stimulation points that elicited motor evoked potentials. They compared the stimulation points with both preoperative and intraoperative reconstructions of the pyramidal tract and found that the intraoperative subcortical stimulation did not correlate with the preoperative reconstruction shown in the navigation system, whereas there was a strong correlation with the intraoperative images. Although these two approaches (comparison with postoperative and intraoperative DTI images) eliminate many of the errors generated by measuring the tract-to-stimulation site distance in the neuronavigation system, there are obvious drawbacks to both of them – in cases in which the postoperative scan is used, the exact stimulation site can only be determined retrospectively as the nearest point of the resection cavity towards the tract. In the case of intraoperative MRI, the procedure requires patient re-positioning for the scanning and the eventual continuation of the

resection, with the possibility of brain shift occurring due to these rearrangements. Both early postoperative and intraoperative DTI scans are prone to susceptibility artifacts at the air-tissue boundary. These artifacts will not be prominent on the anatomical sequences acquired for DTI overlay, often presented in the publications, but they affect the quality of the standard DTI scans tremendously. Moreover, the quality of the DTI scan will be affected by the edema from tissue manipulation; the volume and therefore the borders of the DTI fiber tracts might also be affected if a part of the tract exhibits diffusion characteristics below the set tracking threshold. As a result, DTI fiber tracking will become more operator-dependent because of the need to exclude the "contaminating" artifact fibers in the vicinity of the resection cavity.

The aim of this study was to analyze our single-institution group of patients with intrinsic brain tumors that were operated on with the use of DTT reconstructions of the corticospinal tract in the navigation planning station and the navigation system, to compare the results with intraoperative subcortical stimulation and to analyze the influence of tumor-to-tract distance on the extent of the resection and the short-term postoperative outcome. The study has been approved by an institutional ethics committee. All patients signed a written informed consent regarding their inclusion in this study.

6.1.1 Methods

6.1.1.1 Patients and clinical evaluation

A total of 69 adult patients harboring an intrinsic brain tumor in the vicinity of the pyramidal tract have been included in this study from March 2008 until May 2011. In three patients (cases 13 and 14, 50 and 51, 60 and 61), DTI reconstruction of the pyramidal tract was used in two surgeries (resection and re-resection or in two re-resections); our database therefore includes data on 72 surgical cases. The mean age calculated for the cases was 54.4 years (standard deviation 12.6); there were 36 male and 33 female patients. The cases include 46 high-grade glioma (HGG) resections, 11 resections of metastases and 15 resections of low-grade-gliomas (LGG). In 33 cases, the

patients presented with some preoperative paresis. For short-term outcome analysis, motor functions were evaluated in all patients on the 3rd and 10th postoperative days. If the patient was discharged on the 7-10th day, the examination was performed on discharge. The motor functions were classified as "same", "worse" or "better" based on the presence and the extent of pronator drift over 30 seconds and a muscle strength examination based on the Medical Research Council (MRC) classification. Long term outcomes can be influenced by tumor progression and various other factors, which exceed the scope of this work. Therefore, we are only presenting the long term outcome in cases in which motor deterioration persisted at the 7-10th day evaluation. The motor functions were marked as "worse" unless a postoperative complication such as an epidural or intracerebral hematoma, or a medical complication or death, occurred in the early postoperative course, modifying the motor functions independently from the surgery – such patients were excluded from the analysis. The relationship between the tumor-to-tract distance (see below) and the deterioration of the motor functions after surgery was statistically evaluated using logistic regression. The probability of the deterioration of motor functions on the 3rd postoperative day in relation to the TTD was also evaluated using a logistic regression model. For the 7-10th day, this analysis was not performed, as it would not be meaningful due to the small number of patients with a persisting deficit in our series.

An overview of the cases, diagnoses, anatomical locations and planned surgery types is shown in Table 1.

N	Sex	Age	Diagnosis	Lesion location	Surgery type
1	M	66	glioblastoma (WHO IV)	right temporo-parieto-occipital (extending around the lateral ventricle)	resection
2	M	62	glioblastoma (WHO IV)	basal ganglia left, extending into the cerebral peduncle	partial resection / biopsy
3	M	54	glioblastoma (WHO IV)	left temporo-occipital	partial resection / biopsy
4	F	60	glioblastoma (WHO IV)	left parieto-occipital (P1 extending subcortically around the lateral ventricle)	partial resection / biopsy
5	F	59	glioblastoma (WHO IV)	left fronto-parietal (semioval center)	resection
6	M	30	oligodendroglioma (WHO II)	right insular (Yaşargil 5A)	resection
7	F	63	glioblastoma (WHO IV)	left fronto-parietal (semioval center)	resection
8	F	70	glioblastoma (WHO IV)	left frontoparietal, 2 enhancing lestions (1. left frontal precentral, 2. left frontal postcentral)	partial resection / biopsy
9	F	45	oligodendroglioma (WHO II)	left fronto-temporo-parietal	partial resection / biopsy
10	M	50	glioblastoma (WHO IV)	left frontal (semioval center)	partial resection / biopsy
11	F	55	glioblastoma (WHO IV)	right parietal (P1, semioval center)	resection
12	F	43	astrocytoma (WHO II)	right frontal (F1, semioval center)	resection
13	F	64	glioblastoma (WHO IV)	right temporoparietal (T1, precentral gyrus, at the level of the lateral ventricle on axial scans)	re-resection
14*	F	64	glioblastoma (WHO IV)	right temporoparietal (T1, precentral gyrus)	re-resection
15	F	22	astrocytoma (WHO II)	right insular (Yasargil 5A)	re-resection
16	M	61	oligodendroglioma (WHO II)	right insular (Yasargil 5A)	resection
17	M	48	glioblastoma (WHO IV)	cystic tumor, right frontal, temporal and parietal	resection
18	M	56	glioblastoma (WHO IV)	left temporal pole, extending into the subcortical white matter dorsally and medially	resection
19	F	59	glioblastoma (WHO IV)	right parietal, subcortical	resection

				under the postcentral gyrus laterally	
20	F	29	oligoastrocytoma (WHO II)	right insular (Yasargil 5A)	resection
21	F	63	metastasis,lung carcinoma	right frontal under F1-F2 supraventricular in the semioval center	resection
22	M	25	astrocytoma (WHO II)	right parietal operculum, extending into the precentral gyrus cranialy and subcortical white matter medialy	resection
23	F	69	glioblastoma (WHO IV)	right parietal, postcentral gyrus cortical and subcortical	resection
24	M	36	anaplastic astrocytoma (WHO III)	right insular (Yasargil 5B)	re-resection
25	F	61	glioblastoma (WHO IV)	right parietal, P1 cortical and subcortical extension	resection
26	M	53	glioblastoma (WHO IV)	insular left (Yasargil 3A)	resection
27	F	61	anaplastic oligodendroglioma (WHO III)	left frontal F1-F2 cortical and subcortical	resection
28	M	35	anaplastic oligodendroglioma (WHO III)	right parietal P1-P2 infiltrating the subcortical white matter towards the right lateral ventricle	resection
29	F	66	glioblastoma (WHO IV)	left frontal (precentral gyrus with subcortical extension)	partial resection / biopsy
30	M	68	anaplastic oligodendroglioma (WHO III)	left parietal, postcentral gyrus with large extension into the subcortical white matter	resection
31	M	54	anaplastic oligodendroglioma (WHO III)	right frontal, cortical and subcortical, almost whole frontal lobe infiltrated	resection
32	M	59	glioblastoma (WHO IV)	right parieto-temporo-occipital, cortical in T1, propagation into the parietal lobe under P2 a occipital lobe towards the trigone	resection
33	F	58	glioblastoma (WHO IV)	left parietal (subcortical under P2)	resection
34	F	62	metastatis, breast carcinoma	right frontal F1 cortical and subcortical	resection
35	F	25	astrocytoma (WHO II)	right insular (Yasargil 5B)	resection

36	M	56	glioblastoma (WHO IV)	right parietal - cortical in precentral operculum, extending posteriorly into the subcortical white matter	resection
37	M	48	metastasis, bronchogenic carcinoma	right frontal F2-F3 large metastasis	resection
38	F	47	glioblastoma (WHO IV)	left temporo-occipital T1-T2 extending to the occipital horn of the lateral ventricle	resection
39	M	63	glioblastoma (WHO IV)	right frontal F1 cortical and subcortical	resection
40	M	45	oligodendroglioma (WHO II)	left parietal (P1-P2 extending towards the sylvian fissure)	resection
41	M	79	metastasis, colorectal carcinoma	left parietal, postcentral gyrus cortical - subcortical	resection
42	M	60	glioblastoma (WHO IV)	right occipito-parietal, extending from the trigone cranially into subcortical parietal lobe	resection
43	F	44	papillary glioneural tumor (WHO I)	left temporooccipital, cystic tumor with solid node, located subcortically in the temporal lobe with cysts extending parietally	resection
44	M	67	glioblastoma (WHO IV)	right frontal (F2, F1 cortical with extension into the semioval center dorsally)	re-resection
45	M	50	metastasis, malignant melanoma	right frontal (F2 cortical)	resection
46	M	47	metastasis, thymic carcinoma	right frontal, F1 cortical with subcortical extension	resection
47	M	75	metastasis, squamous cell carcinoma, no primary tumor known	right parietal, subcortical in postcentral gyrus, extending into the semioval center ventrally	resection
48	M	41	glioblastoma (WHO IV)	left fronto-parietal subcortical, giant tumor infiltrating the basal ganglia	partial resection, decompression
49	M	56	glioblastoma (WHO IV)	right temporo-occipito-parietal, subcortical T2 extending cranialy into P1 and dorsaly into the occipital lobe around the lateral ventrikle	resection

50	F	60	glioblastoma (WHO IV)	right parietal (cortical in postcentral gyrus and subcortical extension)	resection
51*	F	61	glioblastoma (WHO IV)	subcortical recurrence in the postcentral gyrus extending ventraly into the precentral gyrus	re-resection
52	M	69	metastasis, small cell lung carcinoma	left temporooccipital (T1-T2 extending into the occipital lobe)	resection
53	M	60	glioblastoma (WHO IV)	butterfly glioblastoma, frontal lobes bilateral, major portion right in the semioval center under F1 and F2	resection
54	F	81	glioblastoma (WHO IV)	left parieto-occipital, subcortical, P1-P2 extending around the lateral ventricle into the occipital lobe	resection
55	F	37	anaplastic oligodendroglioma (WHO III)	left parietal (P1-P2 subcortical in the semioval center)	resection
56	F	57	glioblastoma (WHO IV)	left parieto-occipital cortical P2, subcortical extension under P1 and around the lateral ventricle into the trigone	resection
57	M	68	glioblastoma (WHO IV)	right parietal, cingulate gyrus, extending into the corpus callosum to the midline, cranially into the precentral gyrus and F1	needle biopsy
58	M	61	glioblastoma (WHO IV)	left parietooccipital (subcortical, P1-2, extending occipital lobe around the lateral ventricle)	resection
59	F	59	metastasis, lung carcinoma	left frontal (subcortical F2)	resection
60	F	65	glioblastoma (WHO IV)	left parieto-occipital (subcortical, extending from P2 to the occipital lobe)	resection
61*	F	66	glioblastoma (WHO IV)	left parietal (P2-P1 subcortical recurrence)	re-resection
62	M	56	metastasis, lung carcinoma	right parietal (subcortical P1-P2)	resection

63	F	45	astrocytoma (WHO II)	left frontal (cortical F1 precentrally, subcortical extension of the tumor remnant / recurrence)	re-resection
64	M	38	glioblastoma (WHO IV)	left parieto-occipital, cortical in occipital pole, extending into the trigone of the lateral ventricle ventraly, cranially into the P1-2 subcortically	resection
65	F	44	anaplastic astrocytoma (WHO III)	right insular (Yasargil 3B)	resection
66	F	60	glioblastoma (WHO IV)	subcortical, left frontal semioval center supraventricular, main mass under F2, extending under F1	resection
67	M	35	astrocytoma (WHO II)	subcortical, left frontal semioval center supraventricular under F1 and F2	resection
68	F	49	glioblastoma (WHO IV)	right cingulate gyrus frontally, extending cranially into the supraventricular white matter under F1	resection
69	M	49	astrocytoma (WHO grade II)	infiltrating, left mesiotemporal - dentate, parahippocampal, fusiform gyri, temporal pole, compressing the cerebral peduncle, extending into the internal kapsule	partial resection / biopsy
70	M	64	metastasis, lung carcinoma	right parietal, cortical extending into the semioval center (P1 - P2)	resection
71	F	45	astrocytoma (WHO II)	left frontal (cortical F1-F2, semioval center)	resection
72	F	54	astrocytoma (WHO II)	right frontal (cortical F1, semioval center)	resection

Table 1. Overview of the cases. Case pairs 13 and 14, 50 and 51, and 60 and 61 represent 3 patients with two surgeries each; the second case for each of the pairs is marked with an asterisk

6.1.2 DTI acquisition and analysis, volumetric assessment of the resection

Two MRI scanners and imaging protocols have been used as new equipment became available at our hospital during the study. In cases 1 to 41, MRI was performed on a Symphony scanner (Siemens, Erlangen, Germany). DTI scans were acquired with the following parameters: one b=0 s/mm^2 image and 6 diffusion encoding directions at b=1000 s/mm^2, matrix 128x128, FOV 279x279 mm, TR/TE: 10100/96 ms. In cases 42-72, an Avanto scanner (Siemens, Erlangen, Germany) was used to acquire DTI scans with the following parameters: one b=0 s/mm^2 image and 20 diffusion encoding directions at b=1000 s/mm^2, matrix 138 × 192, FOV 276 × 384 mm, TR/TE 8000/94 ms. In each case, a high resolution sagittal or axial T1 image after intravenous contrast administration (for HGGs and metastases) or a T2 (for LGGs) image was acquired in addition to the DTI for use in the navigation system and for the overlay of the DTI-reconstructed fiber tracts. The same type high resolution scan was acquired postoperatively for comparison and tumor remnant measurement, with pre-contrast and post-contrast scans being acquired for enhancing tumors.

A new fiber tracking application also became available during the course of this study at our hospital. In cases 1-16, the preoperative fiber tracking was performed using Volume-One and dTV II (Tokyo University, Japan). The resulting fibers were voxelized, overlaid on the B0 image and imported into the navigation system Treon Plus (Medtronic, Minneapolis, USA). The fiber map was then coregistered with and overlaid onto the T1 or T2 high resolution scan used for navigation. For cases 17-72, StealthViz software (Medtronic, Minneapolis, USA) was used to reconstruct the fiber tracts and export the resulting maps directly into the neuronavigation system. In the cases in which Volume-One and dTV II were used to reconstruct the tract for intraoperative use, the data were analyzed retrospectively using StealthViz after the software became available.

In Volume-One and dTV II, the tracts were reconstructed with the default lower FA threshold of 0.18 and no bending angle threshold. For StealthViz, the parameters of fiber tracking were as follows: seed FA threshold 0.2, fiber tracking termination threshold FA 0.15, bending angle threshold 60 degrees. The fiber tracking was initiated in the subcortical white matter of the precentral gyrus, which was identified based on

anatomical landmarks. The end VOI was placed in the pyramidal tract at the level of the fourth ventricle, as the tract can easily be identified at this level on the color diffusion direction map. Fibers not respecting the known anatomy of the pyramidal tract (corticocerebellar projections, parts of the commissural and association bundles) were manually excluded. The resulting tracts were voxelized as 3D models with a wrapping distance of 1 mm from the displayed fibers; the resulting fiber tract models were then exported for intraoperative use. The preoperative distance between the voxelized tract and the tumor border was measured and recorded (tumor-to-tract distance, TTD). The tumor was then segmented by a manual or semi-manual intensity-based markup method on the anatomical scan, and the preoperative volume of the tumor was recorded.

After the surgery, a postoperative high resolution anatomical scan acquired within three postoperative days was added to the saved fiber tracking session and coregistered with the preoperative scans. If a tumor remnant was detected on T2 (LGGs) or by comparing pre- and postcontrast T1 scans (HGGs and metastases), it was segmented and the volume of the tumor remnant recorded for comparison. The thickness of the remnant (TR) in the direction towards the displayed fiber tract was measured as the minimum remnant thickness in the axial plane detected on postoperative scans. The values of the distances measured were rounded to whole millimeters. The fiber tracking, volumetry and the measurements of TTD and tumor remnant thickness are documented in Figures 1 and 2.

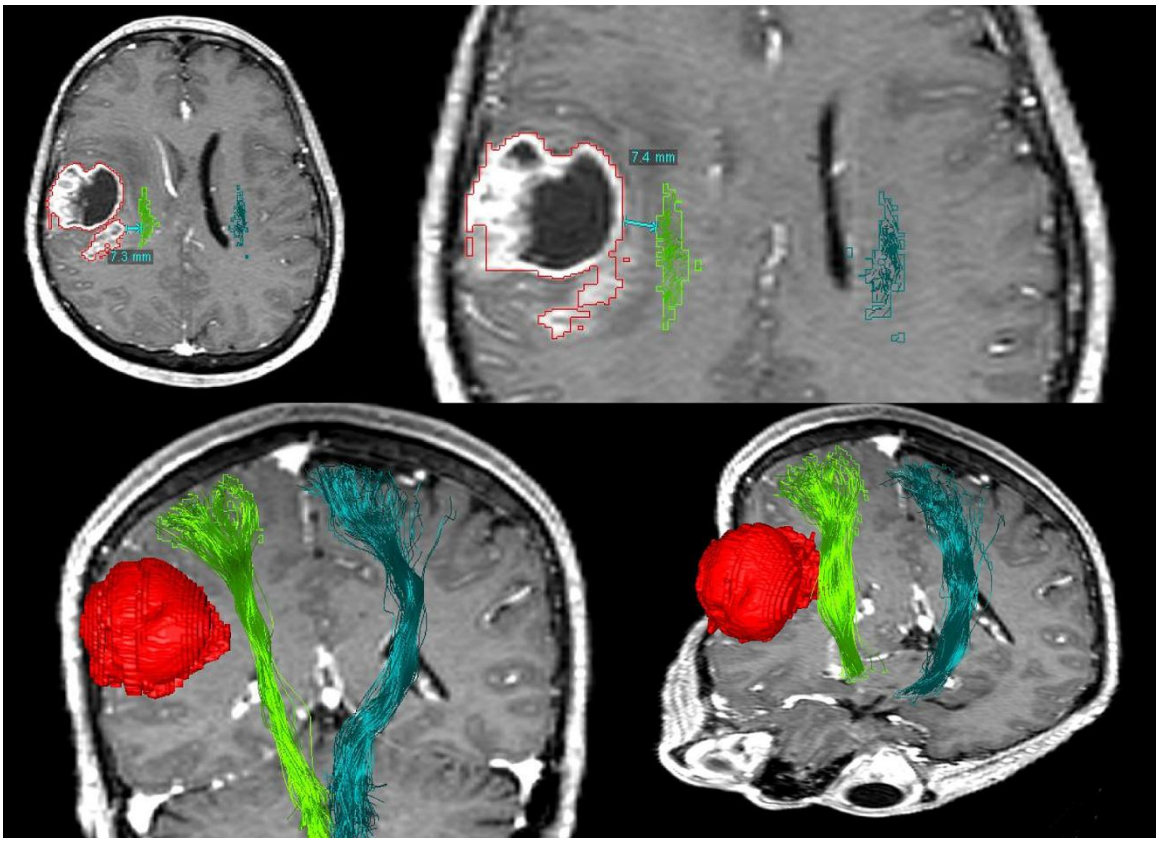

Figure 1. Case 25. Upper row – measurement of the tumor-to-tract distance (TTD) in two slices on axial scans, the smallest value was rounded to whole millimeters and used for the analysis; Lower row – 3D view of the reconstructed tracts; note the disfiguration of the anatomy of the pyramidal tract in the right hemisphere

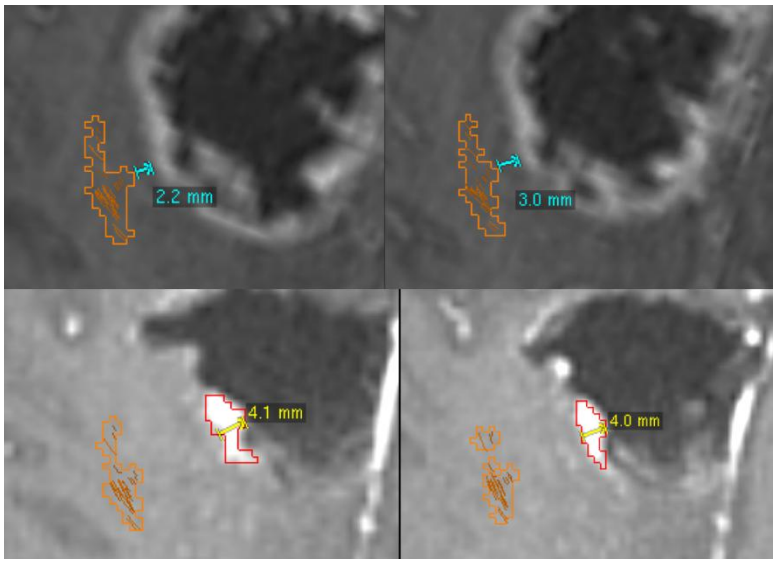

Figure 2. Case 68. A tumor remnant was visible on the postoperative scan after the resection was stopped because of positive stimulation. Upper row – two measurements of the TTD, the smaller value was used for the analysis. Lower row – measurement of the tumor remnant thickness (TR). Note that the pyramidal tract shown in this image is a preoperative reconstruction; a significant brain shift with collapse of the resection cavity is obvious, and the image of the tract was only used to determine the direction in which the tumor remnant should be measured.

The association between the TTD and the extent of resection (as a % value of the preoperative volume) was evaluated by categorizing the value of TTD into 5 groups and performing a Kruskal-Wallis test. Ten cases in which a partial resection or biopsy was planned and performed were excluded from this comparison.

6.1.3 Comparison with direct electrical subcortical stimulation

The surgeons used either direct electrical stimulation both on the cortex and in the subcortical white matter or transcranial MEP monitoring. Transcranial MEP monitoring was used mainly in insular gliomas, and the decrease in MEP amplitude could be attributed to motor tract compromise or to vascular compromise (during manipulation with the M2-M3 branches of the ACM due to vasospasm). Moreover, it would be

unsystematic to include both modalities in the comparison. The data on MEP amplitude decrease were therefore not used for comparison with DTI-derived pyramidal tract position.

Direct electrical stimulation was performed using an Ojemann stimulator in 36 cases. After a craniotomy, exploratory stimulation of the cortical surface around and above the tumor was performed to verify the position of the motor cortex. After that, the tumor resection progressed in the usual manner; the subcortical resection wall surface was stimulated periodically to check for the presence of motor fibers. Current intensities of 4 to 10 mA were used based on the choice of the surgeon, starting gradually from a lower value (4 or 6 mA) and if no motor response was elicited, increasing the current intensity stepwise to 8-10 mA. Care was taken to stimulate the resection wall precisely, focusing mainly on the surface in the direction of the pyramidal tract displayed in the navigation system. If a motor response in the extremities was elicited, the resection was stopped in this direction. For simplicity, cases in which a motor response was or was not elicited will be referred to as cases with a "positive" or "negative" stimulation result further in the text. We did not measure the distance between the stimulation site and the tract in the navigation system.

For each case, two distances of the subcortical stimulation point from the pyramidal tract were measured based on the preoperative and postoperative MRI scans. The first value compared with the subcortical stimulation was the TTD. To correct for differences in tumor resection extent, a second value representing the distance of the stimulation point from the pyramidal tract was calculated as TTD plus the tumor remnant (TR) measured on the postoperative high resolution scans. This value is mentioned as TTD+TR further in text. These continuous values (in millimeters) were compared with the categorical result of the stimulation (positive or negative) statistically. The relationship of the TTD and TTD+TR to the stimulation result was then evaluated using logistic regression; odds ratios and log odds ratios were computed for the created models, and the probabilities of positive stimulation were computed for a range of TTD and TTD+TR distances. In addition, the maximum TTD and TTD+TR values were determined, above which no positive stimulation results were obtained in our series.

Statistica software (Statsoft, Tulsa, USA) was used for the statistical analyses. Values of $p<0.05$ were considered to be significant for all tests.

6.2 Results

6.2.1 Comparison of the tract-tumor distances with the results of the subcortical stimulation

The average TTD was 5.9 mm, standard deviation (SD) 6.3 mm, range 0-30 mm. For the TR the average value was 3.3 mm, SD 4.9 mm, range 0-23. The corrected value TTD+TR averaged 9.2 mm, SD 7 mm, range 0-40 mm. The use of subcortical stimulation, the TTD, TR and TTD+TR values and the tumor volumes as measured on the pre- and postoperative high resolution scans, together with the computed resection extent (discussed in the text below) for each case, are presented in Table 2.

N	DES used	Motor response elicited	TTD	TR	TTD+TR	TV preoperative (cm^3)	TV postoperative (cm^3)	Resection extent	Motor functions 3rd day	Motor functions 7th-10th day
1	no	-	15	0	15	85.5	0.0	100%	worse due to a complication	
2	no	-	0	7	7	17.6	10.2	42%	worse	worse
3	yes	no	0	12	12	87.7	29.9	66%	same	same
4	no	-	9	5	14	127.9	14.6	89%	same	same
5	yes	yes	0	2	2	7.5	1.2	84%	same	better
6	no	-	9	6	15	54.3	6.5	88%	same	same
7	yes	yes	3	1	4	20.0	2.1	89%	better	better
8	yes	yes	0	4	4	5.4	1.7	69%	same	better
9	no	-	0	18	18	98.6	69.1	30%	same	same
10	yes	yes	0	4	4	15.9	6.6	58%	worse	better
11	yes	yes	0	3	3	23.7	0.7	97%	same	better
12	yes	no	10	0	10	23.6	0.0	100%	same	same
13	yes	no	9	0	9	6.4	0.0	100%	worse	better
14	yes	no	2	6	8	17.5	0.8	96%	same	same
15	no	-	4	10	14	48.5	18.6	62%	same	same
16	no	-	3	0	3	151.6	42.0	72%	same	better
17	no	-	9	0	9	17.4	6.1	65%	same	better
18	no	-	6	12	18	100.1	10.7	89%	better	better
19	yes	yes	0	3	3	48.8	2.9	94%	worse	better
20	no	-	17	23	40	85.7	2.8	97%	same	same
21	yes	no	13	0	13	13.3	0.0	100%	same	same
22	yes	yes	3	3	6	26.9	3.9	85%	worse	same
23	yes	no	4	0	4	22.4	1.0	96%	same	same

N	DES used	Motor response elicited	TTD	TR	TTD+TR	TV preoperative (cm^3)	TV postoperative (cm^3)	Resection extent	Motor functions 3rd day	Motor functions 7th-10th day
24	no	-	1	0	1	11.1	2.2	80%	same	same
25	no	-	7	0	7	29.5	0.0	100%	same	same
26	no	-	7	0	7	2.5	0.0	100%	same	same
27	yes	no	0	14	14	156.6	12.4	92%	same	same
28	no	-	0	6	6	16.5	2.3	86%	worse	worse
29	yes	yes	0	3	3	5.0	2.1	58%	worse	same
30	yes	no	5	0	5	75.9	0.0	100%	better	better
31	yes	no	14	5	19	159.4	54.9	66%	same	same
32	no	-	15		15	41.9	0.0	100%	same	same
33	no	-	16	0	16	10.6	0.0	100%	same	same
34	yes	yes	2	0	2	3.7	0.0	100%	same	same
35	no	-	0	8	8	76.1	10.3	87%	same	same
36	yes	no	2	0	2	9.9	0.0	100%	same	same
37	no	-	4	0	4	61.9	0.0	100%	same	better
38	yes	yes	8	0	8	132.3	0.0	100%	worse	worse
39	yes	yes	3	0	3	31.6	0.0	100%	worse	better
40	yes	no	0	12	12	66.7	13.3	80%	same	same
41	no	-	0	0	0	5.2	0.0	100%	worse	better
42	no	-	0	0	0	45.0	1.0	98%	worse	same
43	no	-	20	0	20	1.8	0.0	100%	same	same
44	no	-	20	0	20	54.6	0.0	100%	same	same
45	no	-	7	0	7	41.3	0.0	100%	same	same
46	no	-	6	0	6	41.2	0.0	100%	same	same

N	DES used	Motor response elicited	TTD	TR	TTD+TR	TV preoperative (cm^3)	TV postoperative (cm^3)	Resection extent	Motor functions 3rd day	Motor functions 7th-10th day
47	yes	yes	2	0	2	13.1	0.0	100%	better	better
48	no	-	7	6	13	141.3	6.4	96%	perioperative death	
49	yes	no	6	5	11	53.3	14.2	73%	better	better
50	yes	yes	2	0	2	10.8	1.2	89%	same	same
51	yes	yes	0	0	0	25.3	1.7	93%	same	same
52	no	-	12	0	12	12.3	0.0	100%	perioperative death	
53	no	-	9	2	11	88.5	8.6	90%	perioperative death	
54	no	-	8	0	8	18.9	0.0	100%	same	same
55	yes	no	2	7	9	59.9	11.4	81%	worse	same
56	yes	no	7	3	10	39.1	10.0	74%	better	better
57	no	-	0	0	0	48.4	48.4	0%	same	same
58	yes	no	6	0	6	21.3	3.9	82%	same	same
59	yes	yes	2	0	2	18.0	0.0	100%	better	better
60	no	-	20	0	21	18.5	0.0	100%	same	better
61	no	-	10	0	10	20.2	2.8	86%	same	same
62	no	-	12	0	12	36.0	0.0	100%	same	same
63	yes	no	9	0	9	13.9	0.0	100%	worse	same
64	no	-	15	0	15	85.1	0.5	99%	same	same
65	no	-	6	6	12	19.2	4.0	79%	same	same
66	yes	yes	2	2	4	20.7	0.5	98%	same	same
67	yes	yes	4	1	5	46.2	1.1	98%	same	same
68	yes	yes	2	4	6	68.3	2.4	97%	worse	same
69	no	-	0	14	14	73.8	17.4	76%	same	same

N	DES used	Motor response elicited	TTD	TR	TTD+TR	TV preoperative (cm^3)	TV postoperative (cm^3)	Resection extent	Motor functions 3rd day	Motor functions 7th-10th day
70	no	-	30	0	30	20.5	0.0	100%	better	better
71	yes	no	0	13	13	88.9	53.1	40%	worse	worse
72	yes	no	2	6	8	61.4	4.6	92%	same	same

Table 2. Overview of the results . DES – direct electrical stimulation, TV – tumor volume, TTD – tumor-to-tract distance, TR – tumor remnant thickness

Out of the above-defined 36 surgical cases with subcortical stimulation, a motor response was elicited in 18 patients. In our series, a positive stimulation was obtained only in patients in whom both distances (TTD and TTD+TR) were less than or equal to 8 mm (highest value in case 38). In addition, logistic regression models were created for the comparison of TTD and TTD+R with the results of the subcortical stimulation. The model for TTD was computed as $ln\ (o(\text{TTD})) = 0.9438 – 0.3030 \times \text{TTD}$. The model was significant ($p<.01$); the odds ratio was 10. The odds ratio representing the influence of the unit change of TTD was computed as $o(x+1)/o(x) = e^{-0.3030} = 0.7386$. The quality of the prediction in the form of a contingency table is presented in Table 3.

	Predicted negative	Predicted Positive	Percent Correct
negative stimulation	10	8	55.6
positive stimulation	2	16	88.9

Table 3. Contingency table of the logistic regression model created for the TTD

Probability of a positive stimulation was computed for values of TTD in the range of 1-20. The resulting probability values are presented in Table 4, graphical representation in Figure 3.

TTD	0	1	2	3	4	5	6	7	8	9	10	11	12	13	14
P	0.72	0.65	0.58	0.51	0.43	0.36	0.29	0.24	0.19	0.14	0.11	0.08	0.06	0.05	0.04
TTD	15	16	17	18	19	20									
P	0.03	0.02	0.01	0.01	<0.01	<0.01									

Table 4. Probabilities of positive stimulation for different TTD distances

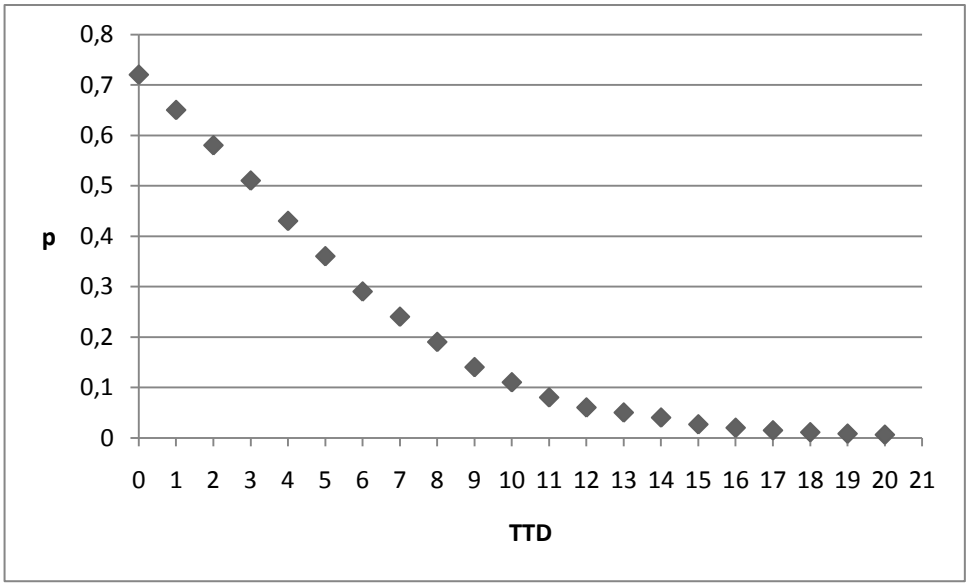

Figure 3. The probabilities of a positive stimulation result during tumor resection in relationship to the TTD distance

A similar logistic regression model was created for the TTD+TR value: ln (o(TTD+TR)) = 4.0509–0.6808×TTD+TR. The model was highly significant ($p<.01$) with an odds ratio of 25. The odds ratio representing the influence of change per millimeter of TTD+TR was $o(x+1)/o(x) = e^{-0.6808} = 0.5062$. The quality of the prediction in this model is presented in a contingency table (Table 5).

	Predicted negative	Predicted Positive	Percent Correct
negative stimulation	15	3	83,3333
positive stimulation	3	15	83,3333

Table 5. Contingency table of the logistic regression model created for the TTD+TR

The probabilities of a positive stimulation result were computed for TTD+TR values ranging from 0 to 14 and are presented in Table 6 and Figure 4.

TTD+TR	0	1	2	3	4	5	6	7	8	9	10	11	12	13	14
P	0.98	0.97	0.94	0.88	0.79	0.66	0.49	0.33	0.20	0.11	0.06	0.03	0.02	0.01	0.00

Table 6. Probabilities of positive stimulation for each value of TTD+TR

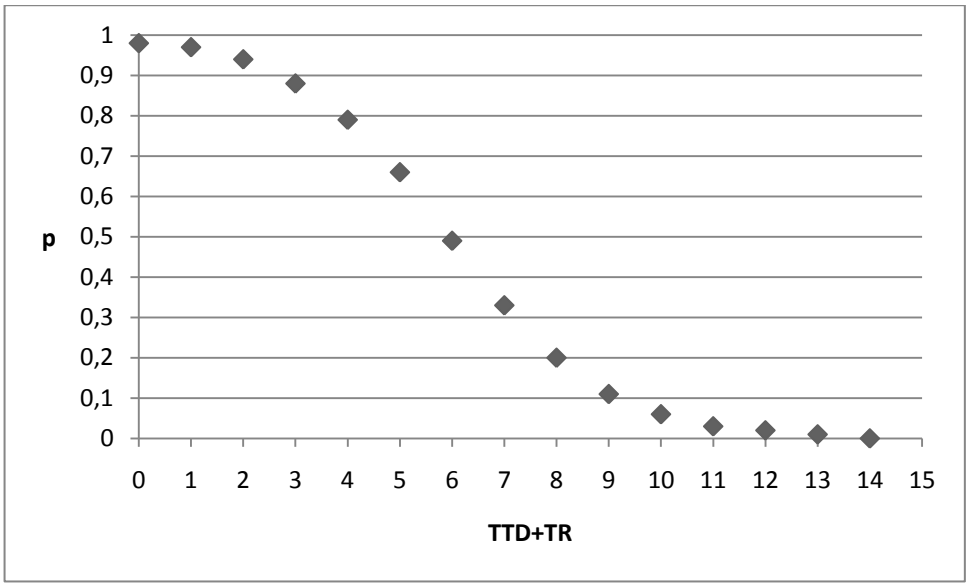

Figure 4. The probabilities of a positive stimulation result during tumor resection in relationship to the TTD+TR

6.2.2 Extent of the resection

The extent of the resection was analyzed in cases in which a gross total resection was planned (n=62). In this subgroup, there were 27 complete resections (44.4%); of these, 13 were high grade gliomas, 3 low grade and all 11 metastases. The results of the volumetric analysis divided into ranges of 90-99%, 80-80% and less than 80% are presented in Table 7.

Tumor type / resection extent	complete	90-99%	80-89%	less than 80%
HGG	13	11	9	5
LGG	3	3	4	3
metastasis	11	0	0	0
Σ	27	14	13	8

Table 7. Volumetric assessment of tumor resection

A Kruskal-Wallis analysis was performed after categorizing the data into 5 groups: TTD=0, less or equal to 3, 7, 12 and more than 12. This analysis did not reveal any significant difference in resection extent between these groups (p=.07). The graphical representation of the relationship between the TTD and resection extent in this subgroup is shown in Figure 5.

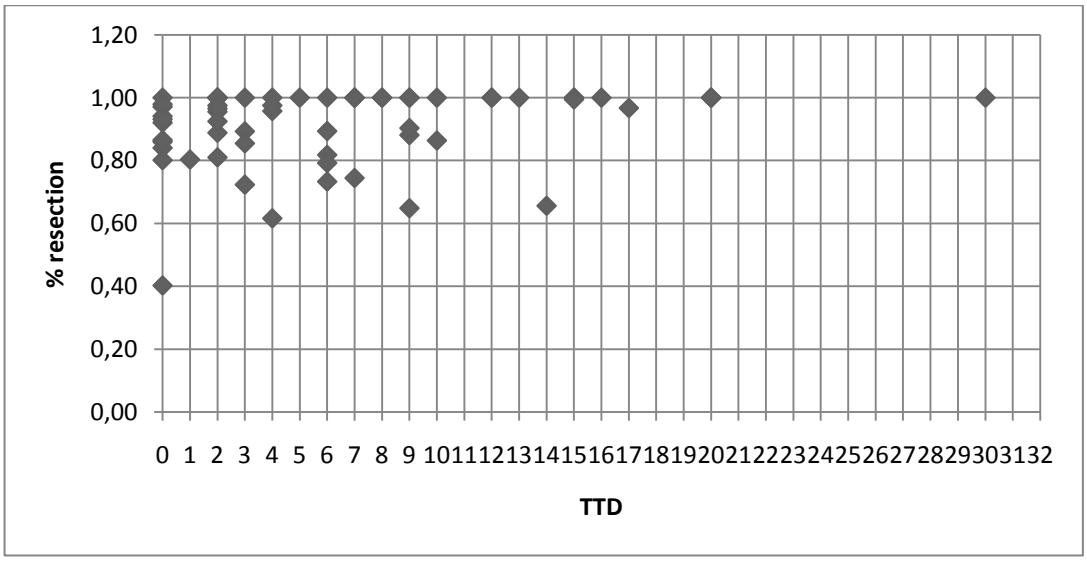

Figure 5. Resection extent in relationship to TTD in n=62 patients who underwent surgery with the intention of a complete resection

6.2.3 Short-term clinical outcome

Among the 72 surgical cases, there were 3 perioperative deaths (4%). Patient 48 with an extensive glioblastoma infiltrating practically the whole left frontal lobe extending into the basal ganglia underwent an extensive partial resection and was awake and oriented with mild expressive aphasia and moderate right side hemiparesis on the third postoperative day; he became unresponsive on the 4th day and died on the 6th postoperative day. No morphological reason was found for this death on autopsy. Patient 52 suffered a myocardial infarction during the resection and died on the third postoperative day. Patient 53 was awake and oriented with marked right side paresis on the third day with a CSF leak from the wound, deteriorated and died on the 15th day from fulminant bacterial meningitis. There was 1 postoperative cerebral hemorrhage in patient 1, which caused a deterioration of motor functions on the 3rd postoperative day; the patient underwent surgical removal of the hematoma and recovered uneventfully. These patients were excluded from further analysis, as the course was not attributable to the tumor resection itself.

In the remaining cases (n=68), the postoperative motor deficit was evaluated as noted above. On the third day, there was a deterioration of motor functions in 15 patients (22%). In 45 patients (66%), the motor functions did not change; improvement was observed in 8 patients (12%).

On the second evaluation (7th – 10th day), the previously deteriorated motor functions improved to a state equal to or better than the preoperative state in 11 of the 15 patients, while in 4 patients (6%) the motor functions remained worsened. The new postoperative paresis was mild and did not alter the functional status of patients 2, 28 and 71, while it was severe in patient 38. In patients 28 and 71, the motor functions were improved to a state equal to or better than preoperative at 3 months follow-up. In patient 2, tumor progression caused a further deterioration at 3 months; patient 38 did not attend the scheduled follow-up. In 20 patients (29%), the motor functions improved and in 43 patients (63%), the motor functions were the same compared to the preoperative examination. An overview of the short term clinical course is presented in Table 2. The logistic regression model created for the relationship between 3rd day deterioration and TTD was found to be significant (p=.001). The probabilities in this model were under 50% even for TTD=0. However, a distinct trend towards deterioration in patients with a smaller TTD was observable. The

probabilities for each TTD value and a graphical representation are shown in Table 8 and Figure 6.

TTD	0	1	2	3	4	5	6	7	8	9	10	11	12	13	14
p	0.38	0.33	0.27	0.23	0.18	0.15	0.12	0.10	0.08	0.06	0.05	0.04	0.03	0.02	0.02

Table 8. Probabilities of early transient postoperative deterioration in relationship to TTD

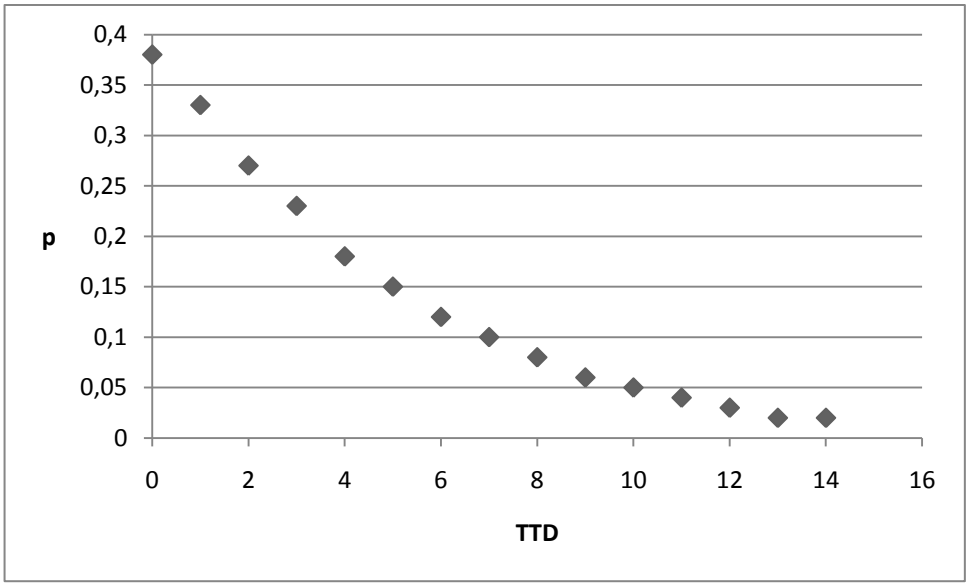

Figure 6. Probability of early (3rd day) postoperative deterioration of motor functions in relationship to TTD

6.3 Discussion

We have observed several interesting relationships in our analysis. The probability of eliciting a motor response during subcortical stimulation depends on the distance between the tumor and the DTI reconstruction of the pyramidal tract measured on preoperative scans. This is what the first logistic regression model tells us – not correcting for any errors that may occur in the process, including the presence of a tumor remnant between the stimulation point and the starting point of TTD

measurement, the tumor border. This observed relationship might be dependent on the surgical tactics employed. At our department, we try to maximize the extent of resection even in cases where only a partial resection is deemed feasible, using subcortical stimulation where appropriate for eloquent tissue protection. In the case of less aggressive surgical tactics, a similar relationship would be hard to observe. We can see that the model predicts a positive stimulation result with high accuracy; however, it is not so successful in predicting negative stimulations, which might again be caused by the presence of the tumor remnant. In absolute numbers, we have not elicited a motor response with subcortical stimulation in any patient with a TTD larger than 8 millimeters; however, the model predicts probabilities that are negligible (<0.01) only for tumors located at least 19 mm from the displayed fiber tract.

The second parameter, TTD+TR, is calculated as the tract-to-tumor distance corrected by adding the tumor remnant thickness observed on postoperative scans in the direction of the original tract depiction, and in our opinion represents a more accurate approximation of the distance between the stimulation point and the pyramidal tract. We might see that the probability is high (bordering on certainty) for distances smaller than three millimeters. This great concordance between the DTI tracking and the subcortical stimulation confirms the accuracy of the DTI pyramidal tract images. The probabilities decrease in a steep slope from three to eleven millimeters and become negligible (less than 0.01) at 14 millimeters. Again, in absolute numbers, we have not encountered a positive stimulation for a TTD+TR value larger than 8 millimeters.

Both models are useful. In general, the first model (based on TTD) informs us about the probabilities of eliciting a motor response during tumor resection based solely on the preoperative tumor-to-tract distance, without correcting for any other factors. The second model (based on TTD+TR) represents the probability of a motor response to stimulation based on a more accurate approximation of the real distance of the stimulation point to the reconstructed tract image, verifying the accuracy of the method.

We have found a good proportion of complete resections given the location of the tumors analyzed in this series. We have not observed a significant trend toward incomplete resections in tumors with shorter TTD distances measured on the preoperative scans in our series, however the analysis neared significance (p=.07). The probability of a temporary deterioration of motor functions showed a trend towards worsening with lower TTD values. Various factors could lead to deterioration, including tumor swelling after partial resection, apart from direct manipulation with the tissue around the tract. However, the information about the greater probability of a temporary deterioration of motor functions can be useful for patient counseling prior to surgery, ameliorating the postoperative negative psychological effects.

In one of the first comparisons between DTI fiber tracking and subcortical stimulation, Berman et al. [19] used a neuronavigation system to stereotactically identify the stimulation points on the preoperative scans, and measured the distances to the displayed fiber tract. The use of navigation to measure the distances during ongoing tumor resection introduces a large spatial error itself due to brain shift; therefore, there is no surprise that the measured average distance was 8.7 mm, range 2-15 mm. However, this article documented the utility of the procedure and the fact that the images of the subcortical tracts in navigation become less and less accurate during the resection, similarly to the navigation images in general. In the same year, Mikuni et al. [57] published a study on 22 patients, 16 of whom underwent awake surgery. The distances between the tumor border and the reconstructed motor fiber tract were measured on preoperative images, and only patients with distances less than 2 cm were included; the authors used subcortical stimulation and electrophysiological monitoring to detect elicited motor evoked potentials (MEPs). They have found that MEPs were elicited at the tumor border when the tumor-to-tract distance was less than 6 mm, a finding similar to ours. For tumor-to-tract distances between 8 and 12 mm, they found a dependence on the anatomical location of the stimulation point – MEPs were elicited only if the white matter was stimulated at the level of the corona radiata and not in the internal capsule or in the brainstem. For patients with a TTD of 13 mm or more, MEPs were not elicited in any case, which also corresponds well with the probabilities determined by our TTD+TR

logistic regression model. They have not discussed the completeness of the resection in their paper. In a very early article, Kamada et al. [21] published a smaller series containing 6 cases of intraaxial tumors, with monopolar stimulation and MEP monitoring, measuring the distances of the stimulation points on the neuronavigation system. They found that they were able to elicit MEPs at distances smaller than 10 mm. In a later paper from the same group [55], a different approach was used, and the stimulation current thresholds were evaluated using distance measurements on early postoperative scans in 40 patients. It should be noted at this point that the intensity and shape of the current spread in the white matter in monopolar stimulation is probably different from that of bipolar stimulation and the results are therefore not universally applicable. However, the paper documented the concordance of both methods and the nonlinear dependence of the stimulation effect on the distance from the tract. In an interesting article, Prabhu et al. [58] documented the use of a navigated monopolar probe in a series of 12 patients. The distance of the probe from the tract at which MEPs were elicited during subcortical stimulation was found to be 7.4 ± 4.5 mm (range 1-19 mm); both preoperative and intraoperative reconstructions of the pyramidal tract were used. In 2 of the 12 cases, in which no subcortical MEPs were elicited, the tip of the probe was at least 19 mm distant from the displayed tract. In a paper documenting the use of intraoperative DTI reconstructions of the pyramidal tract, Maesawa et al. [56] described a series of 28 patients with gliomas, in whom both preoperative and intraoperative images of the tracts were compared with subcortical MEPs. They have found that the range of distances from the stimulation point to the intraoperatively reconstructed pyramidal tract was 0 to 15 mm, average 6.7 mm, as measured on the navigation system. The stimulation current intensity needed to elicit a MEP correlated with the measured distance. They also measured the distances from the stimulation site to the preoperative pyramidal tract reconstruction displayed in the navigation system, and they found that the preoperative reconstructions were located even outside the brain tissue as a result of inward shifting. These distances did not correlate with the current intensities needed to elicit a MEP response.

Various stimulation techniques and various distance measurement methods were described in the above-mentioned literature. Our results support the finding that DTI reconstructions of the pyramidal tract are accurate and reliable and therefore can be

used in the preoperative period for trajectory and resection strategy planning, as well as patient counseling regarding possible postoperative deficits. As supported by all the above-mentioned papers as well as our own results, if the resection is not extended beyond the tumor borders, lesions at a distance over 20 mm from the pyramidal tract on preoperative images should be safely resectable even without the use of subcortical stimulation or MEP monitoring. However, caution must be used, as the tumor borders might not be easily identified intraoperatively. As our results show, with bipolar Ojemann stimulation, the relationship between the distance from the tract and the probability of eliciting a motor response is non-linear and increases steeply only in the close vicinity of the tract. This finding leads to an important clinical implication that the stimulation should be performed meticulously after each thin layer of the tumor has been resected during the procedure.

We are not reporting on the stimulation currents that elicited a motor response in our study, as these were not recorded in all of the cases and current intensities were often increased or decreased according to the choice of the surgeon. The variety of existing stimulation and MEP monitoring techniques limit the usefulness of all the mentioned studies, including our own. Moreover, it has been shown that the conductivity of the tissue may vary even based on the anatomical location of the stimulation point [57]; it is therefore probable that the conductivity within the tumor tissue and on the tumor-brain tissue boundary will also be highly variable. This also explains the fact that the described stimulation point-to-tract distances vary over a relatively large range (up to 20 mm) in the above-mentioned literature. We therefore regard the reporting of probabilities for each mm of distance as a more useful approach.

Another limitation of our study is the fact that it was not possible to determine the exact stimulation point from the postoperative images used for determining the tumor remnant thickness; we have considered the smallest measured distance in the direction of the preoperative depiction of the tract to be the most probable site. We know from the literature and from our own experience that the navigation images become unreliable towards the end of the resection, including but not limited to the images of the DTI reconstructions of the pyramidal tract. The approach used in our study is an approximation; however, we might compare this with the disadvantages of early and late postoperative DTI scans for the distance measurement. In our experience, early postoperative DTI scans suffer from distorting artifacts caused by

retained air as well as by clinically insignificant superficial deposits of blood and material used to cover the resection cavity at the end of the surgery. Moreover, tissue manipulation can lead to increased edema. Although this does not influence the conventional scan used as an overlay for fiber tracking to a great extent, the echo-planar sequences used for DTI are much more prone to suffer from these effects, as can be verified on inspection of the source images. Moreover, motion artifacts are also more likely to occur in the early postoperative period. In tracts located near to the resection cavity, fiber tracking with the same threshold parameters might become unfeasible, making manual adjustments necessary and the distance measurement much more operator-dependent. In late postoperative scans (>2 months from the surgery), the resulting distance can be influenced by glial scar formation or new tumor growth. Both early and late postoperative scans can suffer from artifacts caused by metallic implants commonly used to fasten the bone flap into the craniotomy. Although we do not have experience with intraoperative MRI at our department, the first author of this paper had the opportunity to work with intraoperative scans acquired at 1.5T that, although perhaps the most useful for comparing DTI with electrophysiology, also contain artifacts similar to those on early postoperative scans. Hence, none of the above-mentioned methods of distance measurement can describe reality without error. Therefore, the use of conventional postoperative MRI imaging to determine the tumor remnant as a correction factor for the evaluation of the actual stimulation point to tract distance is an effective approximation.

Many studies have confirmed the anatomical accuracy of DTI reconstructions of the pyramidal tract at this time. The clinical impact is hard to evaluate, as this is an auxiliary technique and the final result of the surgery rests in the hands of the surgeon. Subcortical stimulation remains the gold standard technique for delineating the eloquent tissue. However, given the uncertain conductance of the tissues and the large range of distances measured between the stimulation point and the fiber tract in our and other studies, the question arises whether a residual tumor left behind because of the stimulation could in fact be safely resected. In some cases, the tumor might infiltrate the tract partially, and this part of the tract would probably not be shown on the DTI reconstruction and a resection of such a remnant would lead to a permanent deficit. In other cases, however, we can document a stimulation point

where a response was elicited, that was located at the tumor border and relatively far (>5 mm) from the tract. Therefore, especially in glial tumors, further research should focus on the possibility of more aggressive resections that would be based on the delineation of the eloquent white matter tracts reconstructed from intraoperative DTI.

6.4 Conclusion

The probability of eliciting a motor response by bipolar subcortical stimulation during tumor resection exhibits a non-linear dependence on the tumor-to-tract distance and is negligible in tumors located more than 20 mm from the pyramidal tract on preoperative images. DTI reconstructions of the pyramidal tract are accurate as verified by their concordance with subcortical stimulation. In tumors located close to the pyramidal tract, there was a higher probability of transient motor deterioration after surgery in our series.

7 Anatomy and somatotopy of the pyramidal tract in its supraventricular portion

7.1 Introduction

Many researchers have focused on exploring the anatomy of the pyramidal (or corticospinal) tract with DTI (diffusion tensor imaging) or, as an extension of this technique, with diffusion tensor tracking (DTT). The usual approach makes use of various methods designed to delineate the desired fiber tract based on manual definition of the start and end volumes of interest (VOIs). The setting of the VOIs and therefore the final result of the tracking are therefore largely operator-dependent. After VOI setting, the model of the tract is automatically reconstructed by an algorithm, which can be deterministic, such as the most commonly used fiber assignment by continuous tracking (FACT) or tensor deflection (TEND) algorithms, or probabilistic. Both approaches can produce tract models that are not anatomically accurate and contain portions that do not correspond to the known anatomy of the tract. These portions were aptly called "contaminating fibers" by some authors[20]. The presence of these "contaminating fibers" depends on the algorithm used, threshold settings, DTI data quality and on the setting of the start and end VOIs. To allow meaningful use of the DTT tract models in presurgical planning or in research, these fibers must be excluded manually, introducing more operator-dependent factors and therefore more uncertainty into the technique. Although there are mathematical methods allowing unsupervised tractography [59], these approaches cannot be used routinely in pathological conditions, for instance in tumor patients. A good knowledge of the anatomy of the corticospinal tract is therefore of great importance, allowing the investigator to verify the DTT model of the tract. Recently, there have been publications discussing the localization and the somatotopic organization of the pyramidal tract in the internal capsule as examined by DTT[60; 61],[62] with somewhat contradictory results as to the somatotopy. Let us note that the current spatial resolution of DTT may preclude satisfactory accuracy in discriminating the individual portions of the pyramidal tract at this anatomical level. However, the posterior position of the tract in the posterior limb of the internal capsule was confirmed reliably. The classical description of Déjerine[63] and Foerster[64], which has been repeated in many anatomy textbooks and even in modern publications[65],

localized the corticospinal tract in the anterior half of the internal capsule, with corticobulbar fibers being described in the genu and even slightly extending into the anterior limb of the internal capsule. However, this concept has been challenged by many investigators using various methods (anatomical dissection, explorative deep brain stimulation etc.) and a posterior position or, as the case may be, a posterior shifting of the pyramidal tract during the craniocaudal course in the internal capsule has been described. Substantial evidence of the posterior position of the tract has been neatly summarized in an article by Kretschmann [66] more than 20 years ago. As shown, the organization and the location of motor fibers in the internal capsule have been studied extensively. However, as the internal capsule is surrounded by the basal ganglia, tumors located close to this structure are usually biopsied or only partially resected. Most of the brain tumors that are operated on with the intention of complete resection are located in the supraventricular white matter above the level of the internal capsule, where the pyramidal tract forms a part of the corona radiata. The anatomy of this particular part of the pyramidal tract was recently described by Yamada et al.[67] based on diffusion tensor tractography findings; however, reports are scarce.

The aim of this study was to analyze DTT reconstructions of the tract and the results of subcortical stimulation in patients with tumors located in the supraventricular white matter in order to explore the anatomy of this portion of the tract. Anatomical dissections on formalin-fixed brains using the Klinger technique and a DTI study on healthy hemispheres from our database have been performed to verify our findings.

7.2 Methods

7.2.1 Patients

At our institution, we maintain a database of patients with intrinsic brain tumors where the DTI reconstructions of the corticospinal tract were visualized in the navigation planning station (S7 planning station, Medtronic, Minneapolis, USA) for preoperative planning and intraoperative use in the navigation system (Treon plus, Medtronic, Minneapolis, USA). In this database, we retrospectively identified patients who had undergone a resection of a tumor localized in the supraventricular white matter and in whom subcortical stimulation was used and arm or leg

movement was elicited during the resection. To allow a focused evaluation of the somatotopic organization of the tract, the patients were further selected based on the DTI findings of pyramidal tract position (see below) relative to the tumor and on the response to subcortical stimulation. Only patients in whom a clear posterior or anterior location of the tract to the tumor was seen on DTI were selected for this study; patients with a tumor located directly underneath the precentral gyrus with the main portion of the pyramidal tract medially to the tumor were excluded from the study. Patients in whom subcortical stimulation elicited movement of both extremities were also excluded. In this manner, 13 patients were selected (4 male, 9 female, age 35-75, average 58.9, standard deviation 9.7), operated on between March 2008 and April 2011. The histological diagnoses included 9 glioblastomas, 3 low grade gliomas and 1 metastasis. In patient 1, two enhancing lesions were seen on the preoperative MRI (located in the precentral and postcentral gyri), and partial resection with biopsy was planned; the resection was only performed on the posterior lesion, and the subcortical stimulation was positive, therefore the location of the tumor relative to the tract is listed as "posterior".

The institutional ethics committee did not require a separate consent from the subjects of this retrospective study or a separate approval; however, research on the use of diffusion tensor imaging had already been approved, and the patients signed an informed consent at the time of the imaging.

An overview of the cases, diagnoses, anatomical locations of the tumors and the tract locations relative to the tumor is presented in Table 1.

N	**Sex**	**Age**	**Diagnosis**	**Lesion location**	**Tumor location relative to the pyramidal tract**
1	F	70	glioblastoma (WHO IV)	left frontoparietal, 2 enhancing lestions (1. left frontal precentral, 2. left parietal postcentral)	posterior
2	M	51	glioblastoma (WHO IV)	left frontal (supraventricular white matter)	anterior
3	F	55	glioblastoma (WHO IV)	right parietal (P1, supraventricular white matter)	posterior
4	F	66	glioblastoma (WHO IV)	left frontal (precentral gyrus with subcortical extension)	posterior
5	F	62	metastatis, breast carcinoma	right frontal F1 cortical and subcortical	anterior

6	M	63	glioblastoma (WHO IV)	right frontal F1 cortical and subcortical	anterior
7	M	75	metastasis, squamous cell carcinoma, no primary tumor detected	right parietal, subcortical in postcentral gyrus, extending into the supraventricular white matter ventrally	posterior
8	F	60	glioblastoma (WHO IV)	right parietal (cortical in postcentral gyrus and subcortical extension)	posterior
9	F	61	glioblastoma (WHO IV)	subcortical recurrent tumor in the postcentral gyrus extending ventraly into the precentral gyrus	posterior
10	F	59	metastasis, lung carcinoma	left frontal (subcortical F2)	anterior
11	F	60	glioblastoma, WHO IV	subcortical, left frontal supraventricular white matter supraventricular, main mass under F2, extending under F1	anterior
12	M	35	astrocytoma, WHO grade II	subcortical, left frontal supraventricular white matter supraventricular under F1 and F2	anterior
13	F	49	glioblastoma, WHO IV	right cingulate gyrus frontally, extending cranially into the supraventricular white matter under F1	anterior

Table 1. Overview of the cases. F1 – superior frontal gyrus, F2 – medial frontal gyrus, P1- superior parietal lobule

7.2.2 DTI acquisition and analysis, comparison with subcortical stimulation

Two MRI scanners and imaging protocols have been used as new equipment became available at our hospital during the study. In cases 1 to 6, MRI was performed on a Symphony scanner (Siemens, Erlangen, Germany). DTI scans were acquired with the following parameters: one b=0 s/mm^2 image and 6 diffusion encoding directions at b=1000 s/mm^2, matrix 128x128, FOV 279x279 mm, TR/TE: 10100/96 ms. In cases 7-13, an Avanto scanner (Siemens, Erlangen, Germany) was used to acquire DTI scans with the following parameters: one b=0 s/mm^2 image and 20 diffusion encoding directions at b=1000 s/mm^2, matrix 138 × 192, FOV 276 × 384 mm, TR/TE 8000/94 ms. In each case, a high resolution sagittal or axial T1 image after intravenous contrast administration (for HGGs and metastases) or a T2 (for LGG)

image was acquired in addition to the DTI for use in the navigation system and for the overlay of the DTI-reconstructed fiber tracts.

StealthViz software (Medtronic, Minneapolis, USA) was used to reconstruct the fiber tracts for this study. The parameters of fiber tracking were as follows: seed FA threshold 0.2, fiber tracking termination threshold FA 0.15, bending angle threshold 60 degrees. The fiber tracking was initiated in the subcortical white matter of the precentral gyrus, which was identified based on anatomical landmarks. The end VOI was placed in the posterior limb of the internal capsule; the tract can easily be identified at this level on the color diffusion direction map. Fibers not respecting the known anatomy of the pyramidal tract (corticocerebellar projections, parts of the commissural and association bundles) were manually excluded. The position of the tumor was classified as posterior or anterior relative to the pyramidal tract (see Table 1).

The response to subcortical stimulation together with the extremity in which a movement was elicited were recorded in the above-mentioned database at the time of the surgery. These data were compared with the above-described tumor (stimulation site) position. The Pearson's chi-square test was used to compare the two variables. A p value of 0.05 or less was considered significant for all statistical tests performed in this study.

7.2.3 DTI study of the somatotopy of the supraventricular corticospinal fibers

Separate fiber tracking of arm and leg fibers was performed in 20 healthy (contralateral to tumor) hemispheres from our patient database (10 left hemispheres, 10 right hemispheres). The tracking algorithm starting volume of interest (VOI) was placed in the arm knob identified in the precentral gyrus for arm fibers; the VOI for leg fibers was placed medially. The size of the VOIs was approximately 2x2x2 cm, although individual adjustments were performed with respect to the observed anatomy. Other parameters were the same as described above. The resulting fiber tracts were displayed in axial slices as short portions of 2 mm above and below the visible slice. Screenshots were acquired in 2 axial sections – at the level of the cingulate gyrus and at the level of the lateral ventricle roof. The position of the arm fibers in relation to the leg fibers on the screenshots was then evaluated by two

investigators, both board-certified neurosurgeons (AH and PV). For both tracts, a "center" of the irregular shape was chosen. The position of the arm fibers was then determined visually as the angle between the horizontal (latero-lateral) line passing through the center point of the leg tract and the line connecting both of the centers (Fig 1). Interobserver reliability was evaluated by correlating the angles measured by the two investigators; in addition, the paired samples Wilcoxon test was used to rule out significant differences between the two investigators. The final value was obtained as an average of the two numbers. The angles are reported in degrees; both absolute values and the difference between the angle at the level of the cingulate gyrus and at the level of the lateral ventricle roof (tract rotation) were evaluated. The difference between the angles at the two above-described levels was also tested using the paired samples Wilcoxon test.

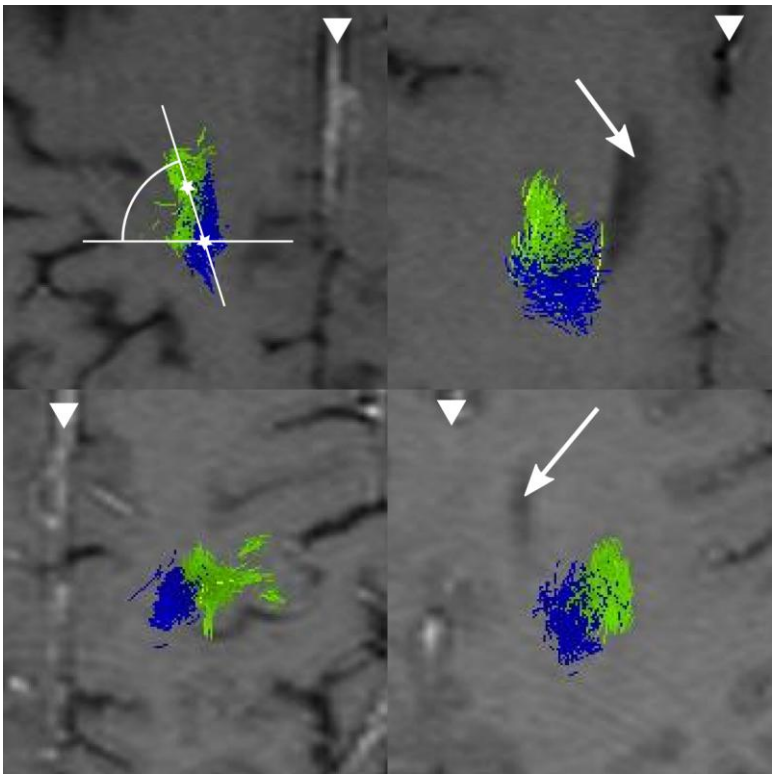

Figure 1. Axial representation of the separately traced arm and leg fibers in two subjects, left – cingulate gyrus level, right – lateral ventricle roof level. Blue – leg fibers, green – arm fibers. Midlines are marked with triangles, ventricles with arrows. Left above – approximate representation of the angle measurement – the angle between the horizontal line and the line connecting the subjectively perceived "center" (stars) of the irregular shape was measured; actual assessment was performed on printed-out screenshots with manual drawing. Note the interindividual difference in the anterior rotation of arm fibers in these two subjects.

7.2.4 Anatomical dissections

To further evaluate the anatomy of the portion of the pyramidal tract located in the supraventricular white matter, we have studied specimens of ten formalin fixed previously frozen human brain hemispheres dissected using the Klinger technique. Seven of these hemispheres had been previously partially dissected according to the procedure published by Türe et al. [68]; the course of the pyramidal tract was studied on these already dissected specimens in the whole length of the tract. Three hemispheres were then dissected in a custom manner, focusing on the pyramidal tract

in its course through the supraventricular white matter. The exact dissection method is described in the results section together with a description of the revealed anatomy. Blunt wooden spatulas were used for most of the dissection; separated fiber bundles were removed by traction using a forceps where appropriate. Sharp instruments were used to amputate parts of the specimens obscuring the view of the area of interest. Although the dissection itself was performed using an operating microscope, the resulting tract surfaces were mostly photographed with a standard camera without magnification, as the final structure of the pyramidal tract is macroscopic. Lateral illumination with the operating microscope's light was used for photography where appropriate, as the lateral light source enhanced the depiction of the dissected surface. The background of the acquired images was darkened or replaced with black color during postprocessing; otherwise, no image manipulation was performed.

7.3 Results

7.3.1 Influence of the position of the stimulation site on the extremity responding to subcortical stimulation

In tumors located anteriorly from the pyramidal tract, the subcortical stimulation caused movement in the upper extremity in 6 cases and in the lower extremity in 1 case. Similarly, in tumors located posteriorly to the pyramidal tract, the subcortical stimulation elicited movement in the contralateral lower extremity in 5 cases and in the upper extremity in 1 case. The association between the location of the stimulation site and the responding extremity was tested with the chi-square test and found to be significant with $\chi^2 = 6.1978$, p-value = 0.01.

7.3.2 Location of arm and leg fibers on DTT reconstructions

The average angle measured as described above was 41.5 degrees at the cingulate gyrus level (15-75, standard deviation 17.3 degrees) and 68.3 at the lateral ventricle roof level (35-105, standard deviation 18 degrees). The measured angle was significantly larger at the ventricle roof level (Wilcoxon paired samples test, $p<.01$), with an average difference between the two levels of 26.75 degrees (0-70, standard deviation 16.7). In fifteen of the twenty subjects (75%), the angle was equal to or

greater than 60 degrees at the level of the lateral ventricle roof. A three-dimensional representation of the observed rotation is shown in Figure 2.

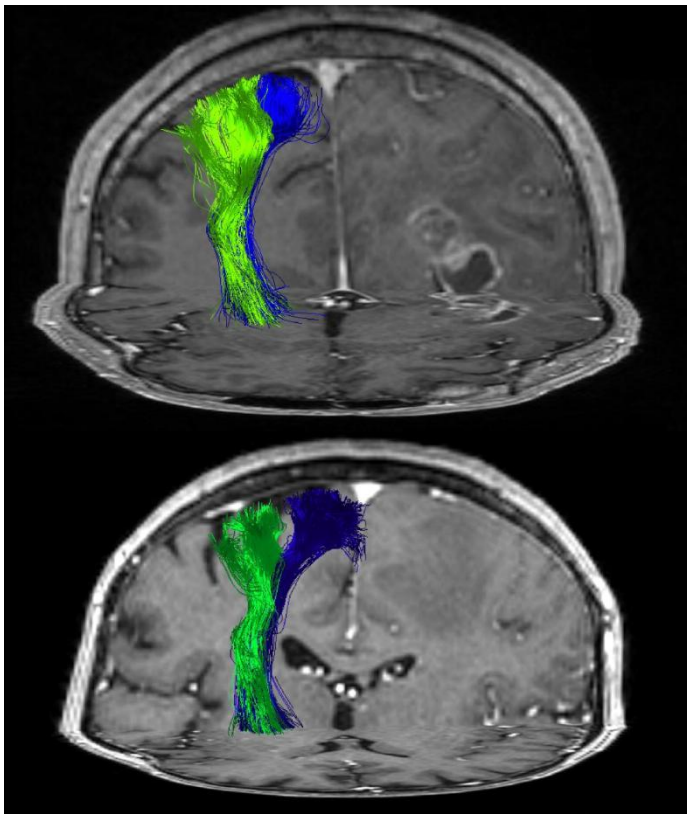

Figure 2. 3D representation of the studied tracts in healthy hemispheres; note the early rotation of the fibers during their course through the supraventricular white matter

The Pearson's correlation coefficient computed for values from the first and second assessing investigator was high and significant (0.82, $p<.01$) for the 40 assessments. The Wilcoxon paired samples test did not show any significant difference between the two investigators (median difference = 0, $p=.3$).

7.3.3 Anatomical dissections

The precentral gyrus was identified on each hemisphere using anatomical landmarks. Dissection commenced at the anterior border of the gyrus and progressed to the depth of the hemisphere. After the gray matter was removed from the precentral sulcus, short U-fibers were found connecting the precentral gyrus to the supplementary

motor area in the superior frontal gyrus (Fig 3). The superior part of the frontal lobe was sharply amputated to enable a better view of the fibers.

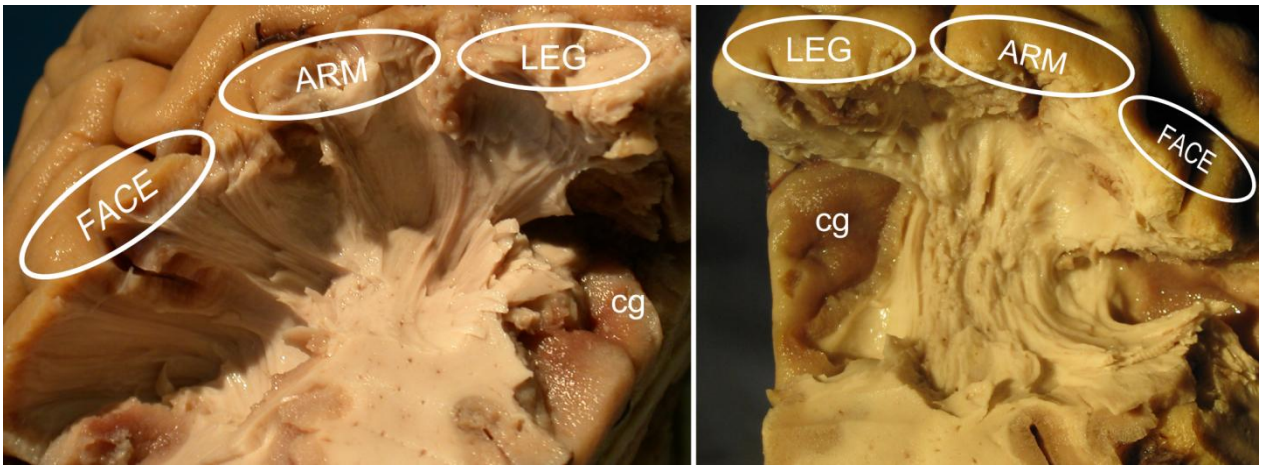

Figure 3. Short U-fibers connecting the precentral gyrus (marked with ovals with a description of the approximate somatotopic representation of the cortex) to the superior frontal gyrus. The frontal gyri are cut above the level of the cingulate sulcus. cg – the gray matter of the cingulate gyrus

The fibers were removed by blunt dissection, revealing another layer under the U fibers turning medially from their origin. The frontal gyri were amputated at the level of the cingulate sulcus. The fibers run in the direction of the corpus callosum, forming a bundle organized in a somatotopic fashion, with fibers originating in the most medial part of the precentral gyrus (leg fibers) entering most posteriorly and fibers originating from the face regions entering most anteriorly. The origin of the most lateral fibers lies below the level of the lateral ventricle, therefore they run upwards above the lateral ventricle roof and then dive downwards to run under the cingulate tract, which crosses these fibers perpendicularly with a rather sharp demarcation (Fig 4).

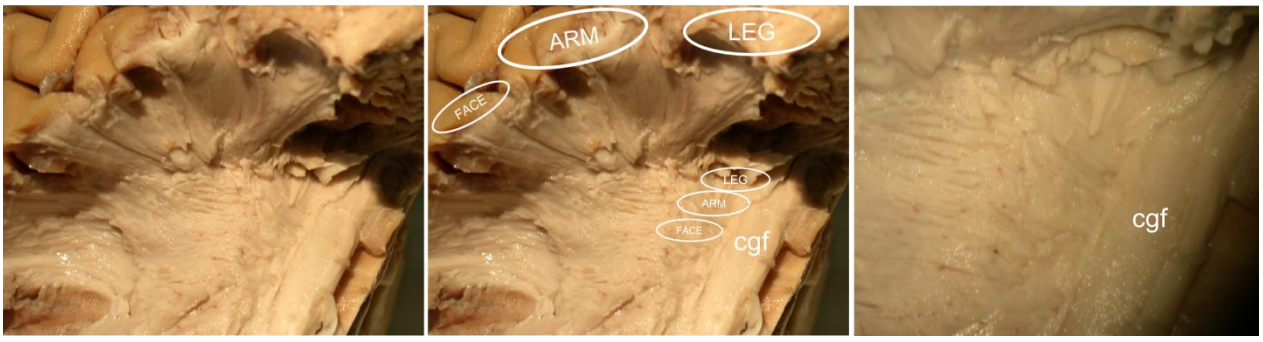

Figure 4. Corpus callosum projections of the precentral gyrus. Left – macrophotograph of the structure, middle – the same with somatotopic description, right – microphotograph of the corpus callosum fibers crossing perpendicularly under the cingulate gyrus fibers (cgf). Note the elevation of the fibers above the lateral ventricle roof.

The cingulate gyrus was bluntly separated from the specimen and sharply removed on the anterior and posterior sides of the dissection cavity, and the corpus callosum became visible. The fibers were then bluntly dissected into the corpus callosum (Figure 5).

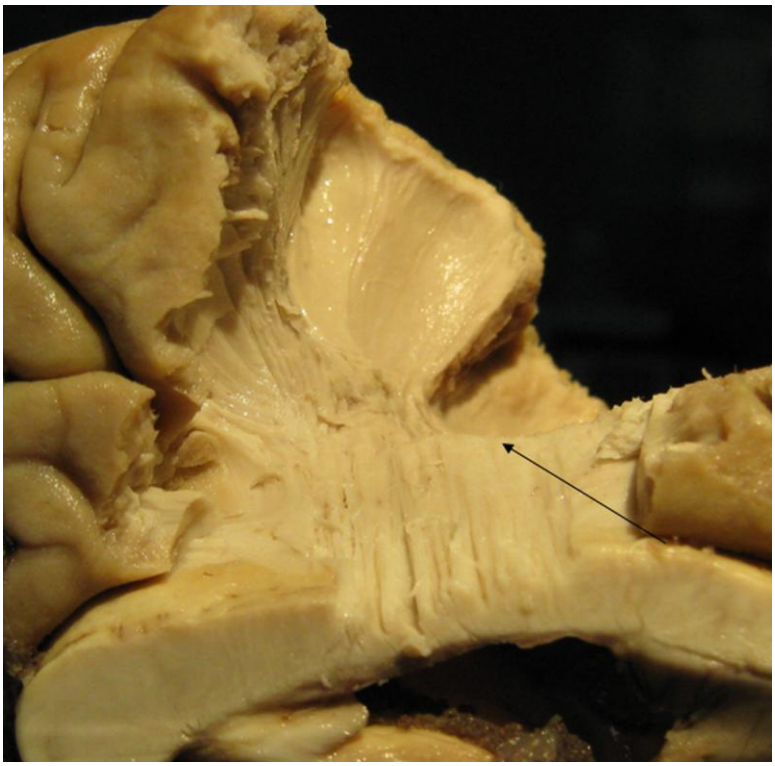

Figure 5. Fibers continuing into the corpus callosum. Note the arching of the fibers above the lateral ventricle (arrow). Cg – cingulate gyrus (sharply cut). Also note the folding arm fan-like structure of the precentral gyrus fibers.

After that, the corpus callosum was cut to reveal the lateral wall of the ventricle. The fibers from the medial parts (leg and arm) were separated easily from the callosal projections and were seen running downwards around the caudate body. However, it was not possible to separate the fibers from the lateral (face) parts of the tract.

The frontal pole was amputated above the thalamus, and the fiber dissection was continued. A structure resembling a folding arm fan was seen, with fibers oriented in an almost antero-posterior fashion at the level of the lateral ventricle roof. An anterior view of the structure is shown in Fig 6.

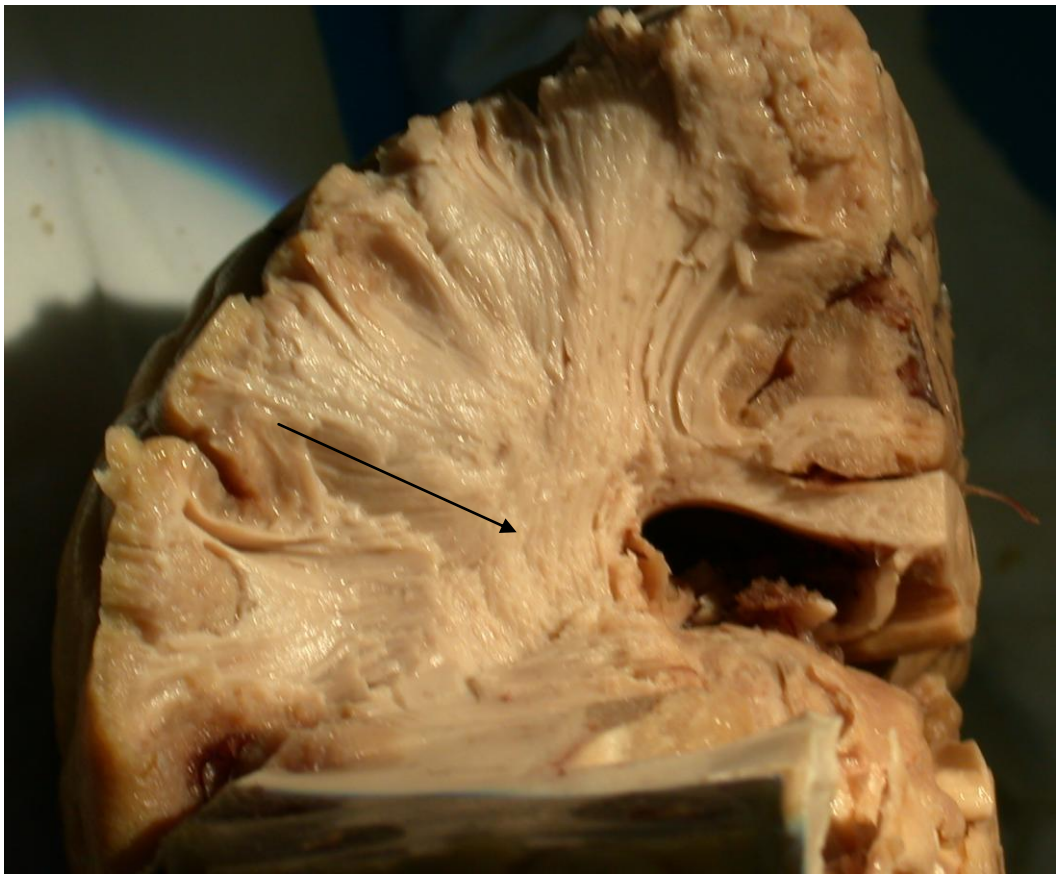

Figure 6. Anterior view of the structure of the pyramidal tract. Note that the most lateral fibers could not be preserved during the resection and are amputated at the level of the corpus callosum (arrow).

7.4 Discussion

We have used three methods to evaluate the course and the somatotopy of the pyramidal tract in the supraventricular white matter. The anatomical dissection confirmed the findings suggested by the comparison of the subcortical stimulation site location in relation to the pyramidal tract with the limb movement elicited – that the rotation of the fibers from a medio-lateral to a postero-lateral configuration takes place largely in the supraventricular white matter. In addition, the anatomical dissections revealed the anatomy of the pyramidal tract as a folding arm fan-like structure with three layers of fibers originating from the precentral gyrus – short U fibers connecting the precentral gyrus to the frontal gyri adjacent to the precentral sulcus, corpus callosum fibers in the middle and the fibers continuing into the internal capsule in the layer most adjacent to the central sulcus. The lateral-to-anterior and medial-to-posterior rotation of the fibers was obvious for both

commissural as well as the projection fibers. According to the results of the DTT part of our study, this rotation takes place during the course of the tract through the supraventricular white matter, and the arm fibers are located almost in front of the leg fibers at the level of the lateral ventricle roof, although interindividual differences exist. However, our assessment might also be influenced by differences in ventricle size.

A DTI study regarding the topographical relations of the pyramidal tract in the supraventricular white matter was published by Yamada et al. [67]. They assessed the course of the pyramidal tract in the lateral view and found that a straight course from the precentral gyrus towards the internal capsule could be observed in the majority of the subjects. This corresponds well to the anatomy we have observed in our study; however, as they have noted, portions of the tract originating from the lateral parts of the tracts are not easily depicted by DTT, consequently a large portion of the subcortical fiber fan of the pyramidal tract was ignored. The somatotopic organization of the tract was not described in their study. Ebeling and Reulen [69] published a dissection study describing the anatomy of the pyramidal tract in great detail. They described a fan-like structure – open against the cortex, shutting towards the posterior limb of the internal capsule – together with a near 90 degree rotation of the fibers from the medio-lateral configuration in the cortex to the postero-anterior configuration in the internal capsule. These findings were confirmed by our study, with further evidence from the stimulation and DTT. As to the comparison of clinical findings with the locations of ischemic lesions on conventional MRI, two articles [70; 71] have analyzed the somatotopic organization of the pyramidal tract in the corona radiata. Both describe an anterolateral to posteromedial organization of the bulbar-arm-leg fibers; however, the lesions described in these papers were not limited to the supraventricular white matter. An interesting study describing the somatotopy of the corpus callosum fibers originating in the precentral gyrus was published by Wahl et al.[72]. They analyzed the somatotopic organization of the fibers originating in the precentral gyrus using DTT and found an antero-posterior bulbar-arm-leg organization of the structure, corresponding to our dissection findings.

The pyramidal tract is the most eloquent structure of the white matter. Philosophical disputes might exist as to what we call eloquent; however, three white matter tracts

have traditionally been considered to be “eloquent” in neurosurgery – the optic radiation, the left arcuate fascicle and the pyramidal tract. Whereas substantial life quality loss can result from damage to the first two structures, permanent damage to the pyramidal tract is associated with the most severe consequences, including further complications should the ensuing deficit prevent the patient from ambulating. A good knowledge of the anatomy of the tract is therefore essential for the neurosurgeon. We have studied the existing literature regarding this subject and found that most studies regarding the somatotopy of the tract describe the topographic relationships in the course through the internal capsule, prompting our effort to investigate the anatomy of the supraventricular portion of the tract.

The subjective visual assessment of the location of arm and leg fibers represents the greatest limitation of this study. The images of the tracts can overlap to some extent, caused by partial volume effects as the technique of DTT suffers from low spatial resolution on clinical MRI equipment. Moreover, the tracking algorithm can produce artifact fibers that do not correspond to actual neural tract anatomy. We have tried to overcome this limitation by including two experienced investigators for the assessment, with rather satisfactory results as to the interobserver reliability. The low number of patients included for the comparison of stimulation site location with motor response represents another limitation of this study. This is caused by the strict criteria, excluding patients with tumors extending below the level of the lateral ventricle roof limit as well as patients in whom a motor response in both the upper and lower extremities was observed. This limitation is outweighed by the clear definition of the cause-response relationship observed in our group of patients.

The Klinger technique is very useful for investigating white matter anatomy and is suitable even for neurosurgeons in training. Individual experience with this technique deepens understanding of the topographical and functional relationships of the dissected tracts. The combination with DTT offers the possibility to explore white matter anatomy while realizing and exploring the limitations of both methods. Given the fact that the structure of large tracts is disputed even in relatively recent publications[73], further exploration of various regions of the white matter is warranted.

7.5 Conclusion

The pyramidal tract undergoes a large part of its rotation from medio-lateral to postero-anterior configuration during its course in the supraventricular white matter, with arm fibers located anteriorly from the leg fibers at the level of the lateral ventricle roof in most subjects. The corpus callosum fibers originating in the precentral gyrus are somatotopically oriented with an antero-posterior face-arm-leg orientation. These commissural fibers originate in the precentral gyrus in front of the projection fibers of the pyramidal tract.

8 The use of diffusion tensor imaging to investigate the aberrant anatomy of the long descending tracts in Chiari III malformation

8.1 Introduction

Chiari III malformation is an extremely rare congenital malformation. The largest series by Castillo et al [74] included 9 cases; Chiari himself described a single case of this type of malformation in his work [75]. Most authors today define a Chiari III malformation as a low occipital or high cervical encephalocele with a brain malformation characteristic of Chiari II malformation [76]. In large malformations, the main neurosurgical concern is the possibility of at least partial resection of the encephalocele allowing primary or delayed closure. The herniated parts of the malformed hindbrain have to be safely identified before or during the resection. However, the treatment options are often limited and depend both on the size of the malformation, the quality of the skin covering the sac and the neurological symptoms the malformation produces. We report a case of a newborn child with Chiari III malformation, in whom herniation of the brainstem and the large descending tracts was delineated with MRI and diffusion tensor imaging (DTI). Using DTI, the position of the descending tracts was ascertained preoperatively, allowing the surgeon to identify the resectable portions of the herniated neural tissue.

8.2 Case Report

A female infant was delivered at term by caesarean section and an occipital mass was noted. Sonographic and routine MRI evaluation revealed a large occipito-cervical encephalocele, and a diagnosis of a Chiari III malformation was established. The condition was not detected prenatally, as the socially underprivileged parents did not attend the regular scheduled check-ups and no sonographic examination was ordered. On examination, the infant was hypotonic, but showed spontaneous movements of all extremities and no lower cranial nerve palsies. The encephalocele was covered by a thick purple tissue layer. On follow-up 6 months later, the neurological findings were the same, except that psychomotor retardation became obvious at this age; the encephalocele sac, however, was markedly enlarged. The MRI examination was repeated with the use of a standard clinical DTI sequence (6 directions, echo planar

sequence, matrix 128x128, FOV 279 mm, TE 96, TR 10100, voxel size 2.2 mm isotropic, scan time 6 minutes 4 seconds), high resolution T1 and T2-weighted scans and MR angiography arterial TOF (time of flight) scans. The anatomical T1 and T2 MRI scans showed an encephalocele containing a dysplastic cerebellum, a part of the occipital lobes, and possibly a large part of the pons and the medulla oblongata. The medulla arched back into the encephalocele upon entering the cranium through the foramen magnum. There was no hydrocephalus on either of the examinations. Temporal lobe herniation into the foramen magnum with dorsal displacement of the medulla, thalamic fusion and corpus callosum agenesis and abnormal gyrification of the telencephalon were also noted. The anatomical scans also showed marked enlargement of the encephalocele, with distention of the CSF spaces within the sac. Compared to the MRI examination performed 6 months earlier, the sac had grown from 37x50 mm (craniocaudal x ventrodorsal, measured as the largest diameter of the sac in the sagittal plane) to 63 x 69 mm. A volumetric analysis was performed, which revealed that the encephalocele sac contained 46.8 cm^3 of neural tissue and 66.5 cm^3 of CSF. The MRA demonstrated a backward arching of the basilar artery, which appeared pulled into the encephalocele sac, suggesting a dislocation of a large part of the brainstem into the sac. For the DTI analysis, StealthViz 1.1 (Medtronic, USA) software was used, the DTI scans were coregistered with the high resolution T1 scans and a DEC (directionally encoded color) map was constructed. The DEC map showed bilateral, large ventrodorsally oriented fascicles continuing from the corona radiata and the internal capsule entering the encephalocele. Three fiber tracking analyses were performed. For the first analysis, the start VOI (volume of interest) was defined in the posterior limb of the internal capsule on both sides. The capsule could not be identified in the anatomical scans; however, the DEC map clearly delineated the position of this structure. The reconstruction was performed with the built-in fiber propagation algorithm. The lower threshold for fractional anisotropy (FA) was set to 0.20 for the start VOI; the same value of 0.20 was set as a threshold for the fiber propagation end. A corona radiata running from the cortex through the internal capsule into the right side of the encephalocele sac was reconstructed on both sides (Figure 1); however, there was no discernable continuation of the fibers from the sac to the spinal cord, as the fractional anisotropy of the malformed encephalocele tissue was too low. The second analysis was

performed using a single VOI placed in the medulla, and it confirmed the backward arching of the medulla fibers as seen on the anatomical scans.

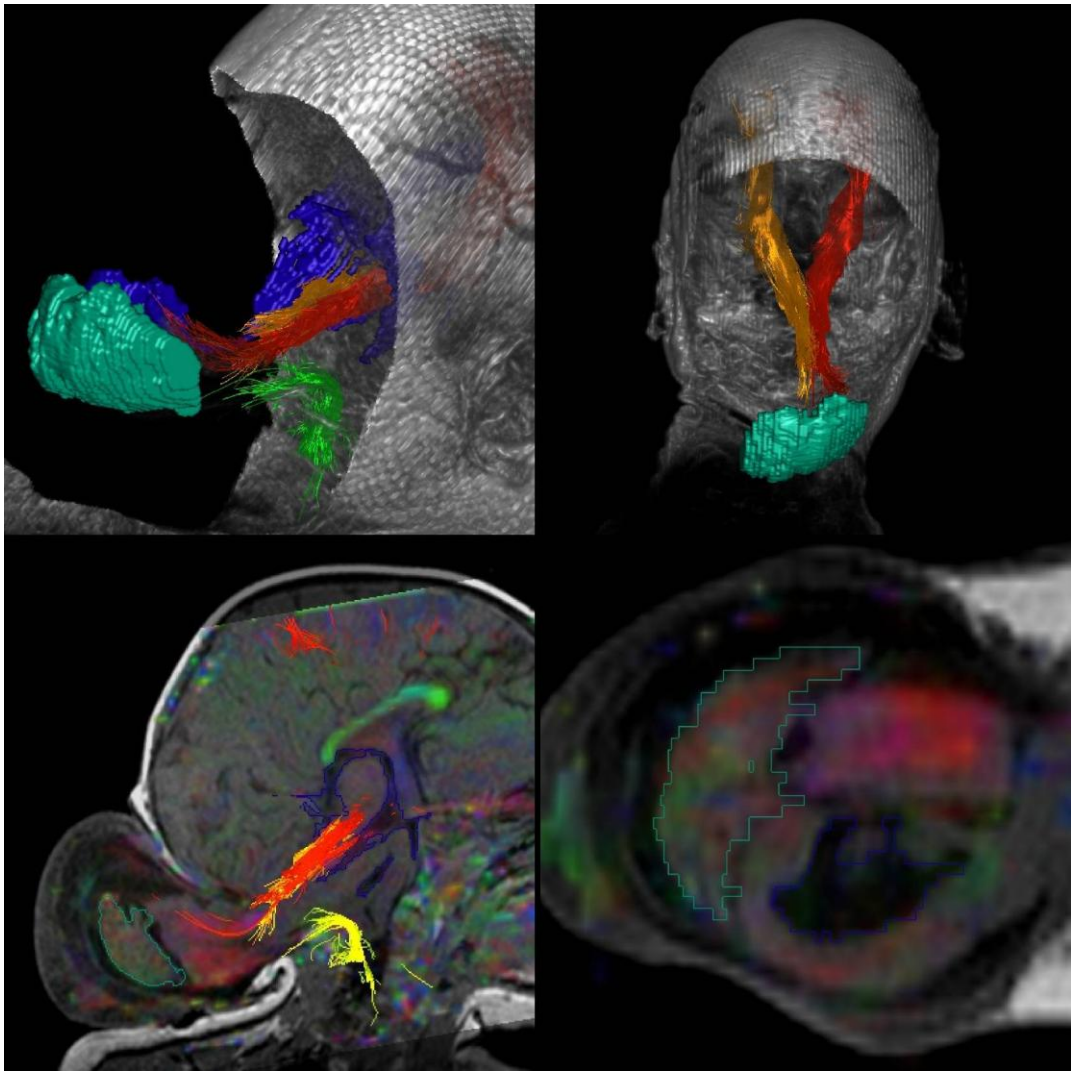

Figure 1 – Top left: 3D reconstruction, yellow and red are the left and right descending tracts entering the encephalocele, green – spinal cord tracking, fibers bending backwards into the encephalocele, cyan – cerebellum, blue – ventricles; Top right: yellow and red – descending tracts passing through the right side of the encephalocele, Bottom left: sagittal projection, yellow - spinal cord fibers; Bottom right: axial section through the encephalocele; note the markedly greater intensity of the DEC map on the right (here top) side of the encephalocele indicating larger fractional anisotropy

The infant was treated by VP (ventriculoperitoneal) shunt insertion, a palliative measure as the prognosis was deemed extremely poor based on the MRI findings. However, the sac continued to grow, and the membranous cover became progressively thinner (Figure 2) and intermittently infected; this was treated by systemic administration of antibiotics, while the baby showed no neurological deterioration and remained in an overall good clinical condition.

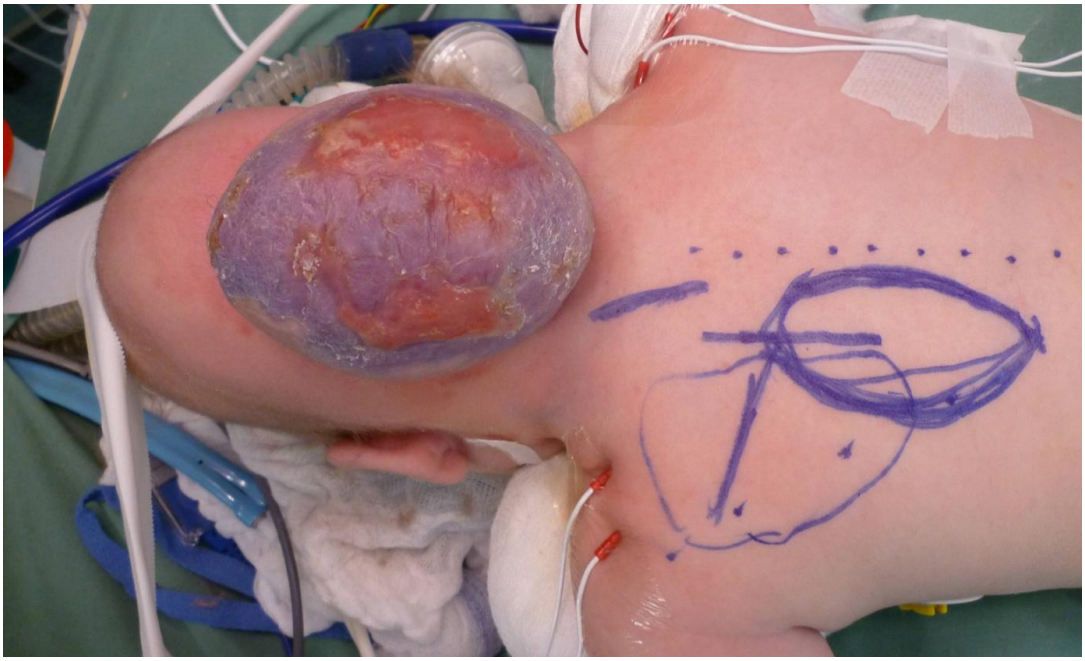

Figure 2 – Preoperative photograph, demonstrating the size and the degradation of the cover of the encephalocele; the planned (but not used) trapezium myocutaneous flap position is marked in blue

Therefore, at nine months of age, a partial resection of the encephalocele was performed, with monitoring of the motor evoked potentials and lower cranial nerves. The dysplastic cerebellum and the dysplastic occipital lobe tissue filling the left side of the sac were partially resected. The resulting size of the encephalocele allowed for primary closure of the skin over the defect, and the planned lower trapezium myocutaneous flap was not used. There was no new neurological deficit noted on the postoperative examination; however, the course was complicated by CSF infection and subsequent leak. This was managed by secondary dural fistula closure, temporary VP shunt removal and antibiotic administration one month after the

surgery; the VP shunt was reimplanted 2 weeks later. At follow-up 4 months after the shunt implantation, the wound had healed completely. Shortly after this follow up, the baby was admitted to a pediatric ward in a peripheral hospital close to the residence of her parents, with respiratory infection and no new neurological symptoms. The throat and nose swab revealed E. coli and N. meningitidis infection and appropriate antibiotics were administered, but the baby died from acute bronchopneumonia on the third day of hospitalization.

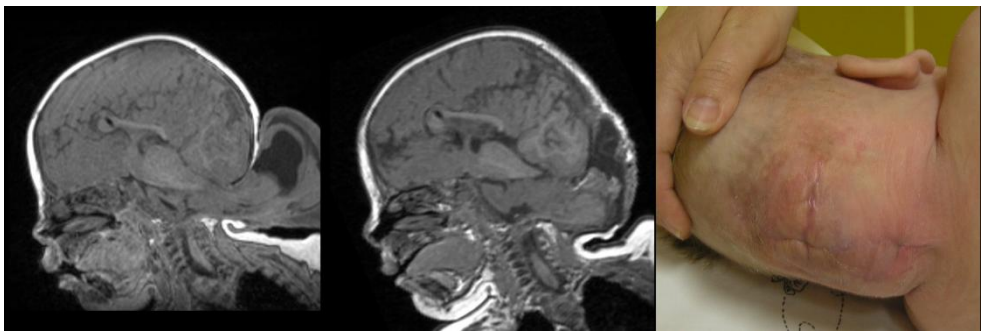

Figure 3 – preoperative (left) and postoperative (middle) T1 sagittal section, postoperative photograph (right)

8.3 Discussion

Chiari type III malformation is more of a curiosity than a mainstream clinical concern. From the surgical perspective, the imaging findings are of key importance, as they provide the surgeon with indispensable information for his decision on treatment.

The usual embryological theory presented in the literature describes the roof of the rhombencephalon being ballooned through the defect of the developing bony structures. The encephalocele then forms a structure similar to the neural plaque of the lumbar meningomyelocele [77]. In the case presented here, the whole rhombencephalon was retracted into the sac, as large portions of the telencephalon were pulled into the virtually nonexistent posterior fossa. The neural structures of the encephalocele then formed the functional pathway between the brain and the spinal cord, which limited the treatment options greatly. As we expected the neurological development of the infant to be hindered by the neural tissue defects associated with this large meningoencephalocele, we decided to implant a VP shunt as a palliative measure, as suggested by previous reports [76], because the documented growth of

the encephalocele sac was caused by CSF accumulation in large part. However, as the infant did not deteriorate neurologically and became endangered only by the enlarging of the sac and the degradation of its cover, we decided to attempt at partial resection and primary closure of the skin defect. At this point, the DTI reconstruction, demonstrating the location of the large tract running from the cortex through the internal capsule to be on the right side of the tract, allowed the surgeon to plan a resection of the non-essential, dysplastic neural tissue in the sac.

The DTI reconstruction was not difficult for the descending tracts running through the posterior limbs of both internal capsules and terminating in the sac on the right side, just anteriorly to the cerebellum. The backward bending of the tracts of the spinal cord upon entering the cranium through the foramen magnum was also easily demonstrated. On the other hand, we were not able to delineate the course of the tracts through the whole encephalocele, as the FA of the tissue was too low; decreasing the lower FA threshold or increasing the maximum allowed angle change for the tracking did not yield meaningful results. Perhaps a different tracking algorithm would have been able to demonstrate the bending of the tracts inside of the malformed tissue; nevertheless, the position of the descending tracts was confirmed by the tracking method used for both the central and the peripheral parts of the tracts. The higher intensity on the FA map also confirmed this result.

In Chiari III malformation, both the imaging and clinical findings may vary from asymptomatic [78] with only a mild defect of the posterior skull base to symptomatic, giant encephaloceles with a poor prognosis. The decision whether to treat surgically and also the timing of the surgery will be based on multiple facts – the quality of the skin covering the encephalocele, the volume of the neural tissue, the vital structures contained within the sac and the neurological deficit. Işik et al [79] recently published a relatively large series of eight Chiari III malformation cases that were treated surgically; this work also includes an extensive review of previously published cases. The authors suggest that maximum possible resection of the neural tissue contained in the encephalocele should be attempted, while keeping in mind that some of the tissue might be functional. In our experience, preoperative DTI can demonstrate the presence and the location of important neural structures in

the sac and help the surgeon evaluate the optimal resection strategy. However, these findings should always be confirmed by intraoperative electrophysiological monitoring during the resection.

8.4 Conclusion

Due to the variety of clinical and imaging findings described in the few published cases of Chiari III malformation, no standard treatment can be recommended; each case should be treated individually. The treatment options include primary surgical closure or VP shunting with delayed surgical closure. Diffusion tensor tractography can help to delineate the position of the descending tracts and decide on the treatment method.

9 Conclusions

The conclusions are sorted in a numbered list. The numbering relates to the objectives defined above.

1. Supraventricular tumors located near to the pyramidal tract induce distant diffusion changes in the tract that are observable more than 15 mm from the tumor border, in the absence of any T2 signal changes. These changes are different in glioblastomas and metastases, with both groups exhibiting significant decrease of the fractional anisotropy. The mean diffusivity (or trace) was significantly increased only in patients with metastases. The mechanisms that contribute to these observed effects are most probably the Wallerian degeneration, increase in extracellular water volume and tumor infiltration. Different mechanisms might take place in different types of tumors.

2. The presence of a gadolinium-based contrast agent causes changes of the observed diffusion parameters as measured by DTI and includes a notable artificial increase of the fractional anisotropy. These effects are strongest in the contrast enhancing areas, but some are also observable in the peritumoral edema and the normal appearing white matter. The observed increase of the fractional anisotropy is caused by disproportionate signal attenuation in the presence of small field distortions resulting from the presence of a paramagnetic material.

3. DTI reconstructions of the pyramidal tract are accurate as verified by their concordance with subcortical stimulation. a. The probability of eliciting a motor response by bipolar subcortical stimulation during tumor resection exhibits a non-linear dependence on the tumor-to-tract distance and is negligible in tumors located more than 20 mm from the pyramidal tract on preoperative images. b. In tumors located close to the pyramidal tract, there is a higher probability of transient motor deterioration after surgery in our series. c. There was no significant association between the tumor-pyramidal tract distance and the extent of the resection.

4. The pyramidal tract undergoes a large part of its rotation from medio-lateral to postero-anterior configuration during its course in the supraventricular white matter, with arm fibers located anteriorly from the leg fibers at the level of the lateral

ventricle roof in most subjects. The corpus callosum fibers originating in the precentral gyrus are somatotopically oriented with an antero-posterior face-arm-leg orientation. These commissural fibers originate in the precentral gyrus in front of the projection fibers of the pyramidal tract.

5. Diffusion tensor tractography can help to delineate the position of the descending tracts and decide on the treatment method in such congenital malformations as Chiari III.

10 References

1. Stejskal EO, Tanner JE. Spin diffusion measurements: spin echoes in the presence of a time-dependent field gradient. The journal of chemical physics 1965; 42: 288.

2. Basser PJ, Mattiello J, LeBihan D. MR diffusion tensor spectroscopy and imaging. Biophys. J 1994; 66: 259-267.

3. Basser PJ, Mattiello J, LeBihan D. Estimation of the effective self-diffusion tensor from the NMR spin echo. J Magn Reson B 1994; 103: 247-254.

4. Inoue T, Shimizu H, Yoshimoto T. Imaging the pyramidal tract in patients with brain tumors. Clinical Neurology and Neurosurgery 1999; 101: 4-10.

5. Coenen VA, Krings T, Mayfrank L, Polin RS, Reinges MH, Thron A, et al. Three-dimensional visualization of the pyramidal tract in a neuronavigation system during brain tumor surgery: first experiences and technical note. Neurosurgery 2001; 49: 86-92; discussion 92-93.

6. Kamada K, Houkin K, Takeuchi F, Ishii N, Ikeda J, Sawamura Y, et al. Visualization of the eloquent motor system by integration of MEG, functional, and anisotropic diffusion-weighted MRI in functional neuronavigation. Surgical Neurology 2003; 59: 352-360.

7. Nimsky C, Grummich P, Sorensen AG, Fahlbusch R, Ganslandt O. Visualization of the pyramidal tract in glioma surgery by integrating diffusion tensor imaging in functional neuronavigation. Zentralbl. Neurochir 2005; 66: 133-141.

8. Nimsky C, Ganslandt O, Fahlbusch R. Implementation of fiber tract navigation. Neurosurgery 2006; 58: ONS-292-303; discussion ONS-303-304.

9. Catani M, Howard RJ, Pajevic S, Jones DK. Virtual in vivo interactive dissection of white matter fasciculi in the human brain. Neuroimage 2002; 17: 77-94.

10. Rimrodt SL, Peterson DJ, Denckla MB, Kaufmann WE, Cutting LE. White matter microstructural differences linked to left perisylvian language network in children with dyslexia. Cortex 2010; 46: 739-749.

11. Stadlbauer A, Pölking E, Prante O, Nimsky C, Buchfelder M, Kuwert T, et al. Detection of tumour invasion into the pyramidal tract in glioma patients with sensorimotor deficits by correlation of 18F-fluoroethyl-L-tyrosine PET and magnetic resonance diffusion tensor imaging. Acta Neurochir 2009; 151: 1061-1069.

12. Stadlbauer A, Nimsky C, Gruber S, Moser E, Hammen T, Engelhorn T, et al. Changes in Fiber Integrity, Diffusivity, and Metabolism of the Pyramidal Tract Adjacent to Gliomas: A Quantitative Diffusion Tensor Fiber Tracking and MR Spectroscopic Imaging Study. AJNR Am J Neuroradiol 2007; 28: 462-469.

13. Romano A, Fasoli F, Ferrante M, Ferrante L, Fantozzi LM, Bozzao A. Fiber density index, fractional anisotropy, adc and clinical motor findings in the white matter of patients with glioblastoma. European Radiology 2008; 18: 331-336.

14. Provenzale JM, McGraw P, Mhatre P, Guo AC, Delong D. Peritumoral brain regions in gliomas and meningiomas: investigation with isotropic diffusion-weighted MR imaging and diffusion-tensor MR imaging. Radiology 2004; 232: 451-460.

15. Saksena S, Nazem-Zadeh M-R, Narang J, Schultz L, Jiang Q, Jain R. Corpus Callosum Wallerian Degeneration in Unilateral Brain Tumors: Evaluation with Diffusion Tensor Imaging. In: Proc. Intl. Soc. Mag. Reson. Med. 19. 2011.

16. Bae MS, Jahng G-H, Ryu CW, Kim EJ, Choi WS, Yang DM. Effect of intravenous gadolinium-DTPA on diffusion tensor MR imaging for the evaluation of brain tumors. Neuroradiology 2009; 51: 793-802.

17. Bae MS, Jahng G-H, Ryu CW, Kim EJ. A systematically designed study to investigate the effects of contrast medium on diffusion tensor MRI [Internet]. J Neuroradiol 2011;

18. Zolal A, Sameš M, Burian M, Nováková M, Malucelli A, Hejčl A, et al. The effect of a gadolinium-based contrast agent on diffusion tensor imaging [Internet]. European Journal of Radiology 2011;

19. Berman JI, Berger MS, Chung S, Nagarajan SS, Henry RG. Accuracy of diffusion tensor magnetic resonance imaging tractography assessed using

intraoperative subcortical stimulation mapping and magnetic source imaging. Journal of Neurosurgery 2007; 107: 488-494.

20. Bello L, Castellano A, Fava E, Casaceli G, Riva M, Scotti G, et al. Intraoperative use of diffusion tensor imaging fiber tractography and subcortical mapping for resection of gliomas: technical considerations. Neurosurgical FOCUS 2010; 28: E6.

21. Kamada K, Todo T, Masutani Y, Aoki S, Ino K, Takano T, et al. Combined use of tractography-integrated functional neuronavigation and direct fiber stimulation. Journal of Neurosurgery 2005; 102: 664-672.

22. Toh C-H, Wong AM-C, Wei K-C, Ng S-H, Wong H-F, Wan Y-L. Peritumoral edema of meningiomas and metastatic brain tumors: differences in diffusion characteristics evaluated with diffusion-tensor MR imaging. Neuroradiology 2007; 49: 489-494.

23. Witwer BP, Moftakhar R, Hasan KM, Deshmukh P, Haughton V, Field A, et al. Diffusion-tensor imaging of white matter tracts in patients with cerebral neoplasm. J. Neurosurg 2002; 97: 568-575.

24. Goebell E, Fiehler J, Ding X-Q, Paustenbach S, Nietz S, Heese O, et al. Disarrangement of fiber tracts and decline of neuronal density correlate in glioma patients--a combined diffusion tensor imaging and 1H-MR spectroscopy study. AJNR Am J Neuroradiol 2006; 27: 1426-1431.

25. Beppu T, Inoue T, Kuzu Y, Ogasawara K, Ogawa A, Sasaki M. Utility of three-dimensional anisotropy contrast magnetic resonance axonography for determining condition of the pyramidal tract in glioblastoma patients with hemiparesis. J. Neurooncol. 2005; 73: 137-144.

26. Lahrmann H, Horvath-Mechtler B, Hitzenberger P, Oberndorfer S, Struhal W, Grisold W. Pyramidal tract degeneration in astrocytoma. J. Neurooncol. 2005; 72: 271-272.

27. Sawlani V, Gupta RK, Singh MK, Kohli A. MRI demonstration of Wallerian degeneration in various intracranial lesions and its clinical implications. J. Neurol. Sci. 1997; 146: 103-108.

28. Thomalla G, Glauche V, Koch MA, Beaulieu C, Weiller C, Röther J. Diffusion tensor imaging detects early Wallerian degeneration of the pyramidal tract after ischemic stroke. Neuroimage 2004; 22: 1767-1774.

29. Werring DJ, Toosy AT, Clark CA, Parker GJ, Barker GJ, Miller DH, et al. Diffusion tensor imaging can detect and quantify corticospinal tract degeneration after stroke. J. Neurol. Neurosurg. Psychiatr. 2000; 69: 269-272.

30. Mori S. Introduction to diffusion tensor imaging. Elsevier; 2007.

31. Moritani T, Ekholm S, Westesson P-L. Diffusion-Weighted MR Imaging of the Brain. Springer; 2009.

32. Giese A, Bjerkvig R, Berens ME, Westphal M. Cost of migration: invasion of malignant gliomas and implications for treatment. J. Clin. Oncol. 2003; 21: 1624-1636.

33. Lu S, Ahn D, Johnson G, Law M, Zagzag D, Grossman RI. Diffusion-Tensor MR Imaging of Intracranial Neoplasia and Associated Peritumoral Edema: Introduction of the Tumor Infiltration Index1. Radiology 2004; 232: 221.

34. Stecco A, Pisani C, Quarta R, Brambilla M, Masini L, Beldì D, et al. DTI and PWI analysis of peri-enhancing tumoral brain tissue in patients treated for glioblastoma. J. Neurooncol 2011; 102: 261-271.

35. Price SJ, Burnet NG, Donovan T, Green HAL, Peña A, Antoun NM, et al. Diffusion tensor imaging of brain tumours at 3T: a potential tool for assessing white matter tract invasion? Clin Radiol 2003; 58: 455-462.

36. Nimsky C, Ganslandt O, Hastreiter P, Wang R, Benner T, Sorensen AG, et al. Preoperative and intraoperative diffusion tensor imaging-based fiber tracking in glioma surgery. Neurosurgery 2007; 61: 178-185; discussion 186.

37. Bammer R. Basic principles of diffusion-weighted imaging. European Journal of Radiology 2003; 45: 169-184.

38. Mori S. Introduction to diffusion tensor imaging. Elsevier; 2007.

39. Yushkevich PA, Piven J, Hazlett HC, Smith RG, Ho S, Gee JC, et al. User-guided 3D active contour segmentation of anatomical structures: significantly improved efficiency and reliability. Neuroimage 2006; 31: 1116-1128.

40. Fox J. The R Commander: A Basic Statistics Graphical User Interface to R. Journal of Statistical Software 2005; 14: 1-42.

41. Ferda J, Kastner J, Mukensnabl P, Choc M, Horemuzová J, Ferdová E, et al. Diffusion tensor magnetic resonance imaging of glial brain tumors. Eur J Radiol 2010; 74: 428-436.

42. Nimsky C, Ganslandt O, Merhof D, Sorensen AG, Fahlbusch R. Intraoperative visualization of the pyramidal tract by diffusion-tensor-imaging-based fiber tracking. Neuroimage 2006; 30: 1219-1229.

43. Fitzek C, Mentzel HJ, Fitzek S, Sauner D, Kaiser WA, Reichenbach JR. Echoplanar diffusion-weighted MRI with intravenous gadolinium-DTPA. Neuroradiology 2003; 45: 592-597.

44. Yamada K, Kubota H, Kizu O, Nakamura H, Ito H, Yuen S, et al. Effect of intravenous gadolinium-DTPA on diffusion-weighted images: evaluation of normal brain and infarcts. Stroke 2002; 33: 1799-1802.

45. Firat AK, Sanli B, Karakaş HM, Erdem G. The effect of intravenous gadolinium-DTPA on diffusion-weighted imaging. Neuroradiology 2006; 48: 465-470.

46. Nimsky C, Grummich P, Sorensen AG, Fahlbusch R, Ganslandt O. Visualization of the pyramidal tract in glioma surgery by integrating diffusion tensor imaging in functional neuronavigation. Zentralbl. Neurochir 2005; 66: 133-141.

47. Nimsky C, Ganslandt O, Fahlbusch R. Implementation of fiber tract navigation. Neurosurgery 2006; 58: ONS-292-303; discussion ONS-303-304.

48. Nimsky C, Ganslandt O, Merhof D, Sorensen AG, Fahlbusch R. Intraoperative visualization of the pyramidal tract by diffusion-tensor-imaging-based fiber tracking. Neuroimage 2006; 30: 1219-1229.

49. Kamada K, Todo T, Masutani Y, Aoki S, Ino K, Morita A, et al. Visualization of the frontotemporal language fibers by tractography combined with functional magnetic resonance imaging and magnetoencephalography. J. Neurosurg 2007; 106: 90-98.

50. Catani M, Jones DK, ffytche DH. Perisylvian language networks of the human brain. Ann. Neurol 2005; 57: 8-16.

51. Chen X, Weigel D, Ganslandt O, Buchfelder M, Nimsky C. Prediction of visual field deficits by diffusion tensor imaging in temporal lobe epilepsy surgery. Neuroimage 2009; 45: 286-297.

52. Kamada K, Todo T, Morita A, Masutani Y, Aoki S, Ino K, et al. Functional monitoring for visual pathway using real-time visual evoked potentials and optic-radiation tractography. Neurosurgery 2005; 57: 121-127; discussion 121-127.

53. Kim CH, Chung C-K, Kim JS, Jahng TA, Lee JH, Song IC. Use of diffusion tensor imaging to evaluate weakness. J. Neurosurg 2007; 106: 111-118.

54. Laundre BJ, Jellison BJ, Badie B, Alexander AL, Field AS. Diffusion tensor imaging of the corticospinal tract before and after mass resection as correlated with clinical motor findings: preliminary data. AJNR Am J Neuroradiol 2005; 26: 791-796.

55. Kamada K, Todo T, Ota T, Ino K, Masutani Y, Aoki S, et al. The motor-evoked potential threshold evaluated by tractography and electrical stimulation. Journal of Neurosurgery 2009; 111: 785-795.

56. Maesawa S, Fujii M, Nakahara N, Watanabe T, Wakabayashi T, Yoshida J. Intraoperative tractography and motor evoked potential (MEP) monitoring in surgery for gliomas around the corticospinal tract. World Neurosurg 2010; 74: 153-161.

57. Mikuni N, Okada T, Nishida N, Taki J, Enatsu R, Ikeda A, et al. Comparison between motor evoked potential recording and fiber tracking for estimating pyramidal tracts near brain tumors. J. Neurosurg 2007; 106: 128-133.

58. Prabhu SS, Gasco J, Tummala S, Weinberg JS, Rao G. Intraoperative magnetic resonance imaging-guided tractography with integrated monopolar subcortical functional mapping for resection of brain tumors. J. Neurosurg 2011; 114: 719-726.

59. Wassermann D, Bloy L, Kanterakis E, Verma R, Deriche R. Unsupervised white matter fiber clustering and tract probability map generation: applications of a Gaussian process framework for white matter fibers. Neuroimage 2010; 51: 228-241.

60. Park JK, Kim BS, Choi G, Kim SH, Choi JC, Khang H. Evaluation of the somatotopic organization of corticospinal tracts in the internal capsule and cerebral peduncle: results of diffusion-tensor MR tractography. Korean J Radiol 2008; 9: 191-195.

61. Holodny AI, Gor DM, Watts R, Gutin PH, Ulug AM. Diffusion-tensor MR tractography of somatotopic organization of corticospinal tracts in the internal capsule: initial anatomic results in contradistinction to prior reports. Radiology 2005; 234: 649-653.

62. Ino T, Nakai R, Azuma T, Yamamoto T, Tsutsumi S, Fukuyama H. Somatotopy of corticospinal tract in the internal capsule shown by functional MRI and diffusion tensor images. Neuroreport 2007; 18: 665-668.

63. Déjerine J. Anatomie des centres nerveux. 1901.

64. Foerster O. Motorische Felder und Bahnen. In: Handbuch der Neurologie. Berlin: Springer; 1936.

65. Jellison BJ, Field AS, Medow J, Lazar M, Salamat MS, Alexander AL. Diffusion tensor imaging of cerebral white matter: a pictorial review of physics, fiber tract anatomy, and tumor imaging patterns. AJNR Am J Neuroradiol 2004; 25: 356-369.

66. Kretschmann HJ. Localisation of the corticospinal fibres in the internal capsule in man. J. Anat 1988; 160: 219-225.

67. Yamada K, Kizu O, Kubota T, Ito H, Matsushima S, Oouchi H, et al. The pyramidal tract has a predictable course through the centrum semiovale: a diffusion-tensor based tractography study. J Magn Reson Imaging 2007; 26: 519-524.

68. Türe U, Yaşargil MG, Friedman AH, Al-Mefty O. Fiber dissection technique: lateral aspect of the brain. Neurosurgery 2000; 47: 417-426; discussion 426-427.

69. Ebeling U, Reulen HJ. Subcortical topography and proportions of the pyramidal tract. Acta Neurochir (Wien) 1992; 118: 164-171.

70. Kim JS, Pope A. Somatotopically located motor fibers in corona radiata: evidence from subcortical small infarcts. Neurology 2005; 64: 1438-1440.

71. Song Y-M. Somatotopic organization of motor fibers in the corona radiata in monoparetic patients with small subcortical infarct. Stroke 2007; 38: 2353-2355.

72. Wahl M, Lauterbach-Soon B, Hattingen E, Jung P, Singer O, Volz S, et al. Human motor corpus callosum: topography, somatotopy, and link between microstructure and function. J. Neurosci 2007; 27: 12132-12138.

73. Türe U, Yaşargil MG, Pait TG. Is there a superior occipitofrontal fasciculus? A microsurgical anatomic study. Neurosurgery 1997; 40: 1226-1232.

74. Castillo M, Quencer RM, Dominguez R. Chiari III malformation: imaging features. AJNR Am J Neuroradiol 1992; 13: 107-113.

75. Chiari H. Über Veränderungen des Kleinhirns in Folge von Hydrocephalie des Grosshirns. Dtsch Med Wochenschr 1891; 27: 1172-1175.

76. Häberle J, Hülskamp G, Harms E, Krasemann T. Cervical encephalocele in a newborn--Chiari III malformation. Case report and review of the literature. Childs Nerv Syst 2001; 17: 373-375.

77. Shuman RM. The Chiari malformations: a constellation of anomalies. Semin Pediatr Neurol 1995; 2: 220-226.

78. Sirikci A, Bayazit YA, Bayram M. The Chiari III malformation: an unusual and asymptomatic variant in an 11-year old child. Eur J Radiol 2001; 39: 147-150.

79. Işik N, Elmaci I, Silav G, Celik M, Kalelioğlu M. Chiari malformation type III and results of surgery: a clinical study: report of eight surgically treated cases and review of the literature. Pediatr Neurosurg 2009; 45: 19-28.

11 List of author's publications

11.1 Publications on the topic of the dissertation (with impact factor)

1. Zolal A, Sameš M., Burian M., Nováková M., Malucelli A., Hejčl A., Bartoš R., Vachata P., Derner M., The effect of a gadolinium-based contrast agent on diffusion tensor imaging. Eur J Radiol 2011 [electronic publication ahead of print] doi:10.1016/j.ejrad.2011.04.074, IF 2,941 (2010)

2. Zolal A., Vachata P., Hejcl A., Malucelli A., Bartos R., Sames M. Identification of the large descending tracts using diffusion tensor imaging in Chiari III malformation. Childs Nerv Syst. 2010, 26(7): 867-70. IF 1,314 (2010)

3. Zolal A., Sameš M., Vachata P., Bartoš R., Nováková M., Derner M.: Použití DTI traktografie v neuronavigaci při operacích mozkových nádorů. Cesk Slov Neurol N 2008, 71/104 (3): 352-357,. IF 0,319 (2008)

4. Kuhnt D, Bauer MH, Becker A, Merhof D, Zolal A, Richter M, Grummich P, Ganslandt O, Buchfelder M, Nimsky C. Intraoperative visualization of fiber tracking based reconstruction of language pathways in glioma surgery. Neurosurgery. 2011 Sep 23. [Epub ahead of print] IF 3.298 (2010)

Impact factor of the publications on the topic of the dissertation: 7.872

11.2 Other publications with impact factor

5. Bartoš R, Vachata P, Hejčl A, Zolal A. Malucelli A, Radovnický T, Posltová M, Cihlář F, Derner M, Sameš M. Vliv funkčního mapování na výsledky operací nízkostupňových gliomů WHO grade II. Cesk Slov Neurol N 2011; 74/107(3): 292-298. IF 0.393 (2010)

6. Sameš M, Radovnický T, Zolal A, Nováková M, Derner M, Vachata P, Bartoš R. Změny na perfuzní počítačové tomografii po konvenčním extra-intrakraniálním bypassu. Cesk Slov Neurol N 2010; 73/106(3): 267-273. IF 0,393 (2010)

7. Zolal A., Sameš M., Vachata P., Bartoš P., Nováková M., Kopáček R., Derner M.: Použití BOLD efektu při vyšetření cerebrovaskulární rezervní kapacity. Cesk Slov Neurol N 2009, 72/105(5): 476-480. IF 0,246 (2009)

8. Sameš M., Zolal A., Radovnický T., Vachata P., Bartoš R., Derner M.: Použití metod magnetické rezonance pro posouzení cerebrovaskulární rezervní kapacity. Cesk Slov Neurol N 2009, 72/105(4): 323-330. IF 0,246 (2009)

9. Bartoš R., Sameš M., Zolal A., Radovnický T., Hejčl A., Vachata P., Cihlář F., Bejšovec D., Petrovický P.: Resekce inzulárních gliomů – volumetrické měření radikality. Cesk Slov Neurol N 2009, 72/105(6): 534-541. IF 0,246 (2009)

10. Sameš M., Bartoš R., Vachata P., Zolal A., Cihlář F., Derner M., Pavlov V.: Hodnocení cebrovaskálární rezervní kapacity po EC-IC bypassu pomocí TCD. Cesk Slov Neurol N 2009, 72/105(4): 359-363. IF 0,246 (2009)

11. Bartoš R., Ceé J., Zolal A., Hejčl A., Bolcha M., Prokšová J., Sameš M.: Extraoperativní mapování pomocí kortikálního gridu před resekcí difuzního oligodendrogliomu v řečově dominantní hemisféře – alternativa „awake kraniotomie“ – kazuistika. Cesk Slov Neurol N 2008 71/104(6): 718-721, IF 0,319 (2008)

12. Bartos R, Jech R, Vymazal J, Petrovický P, Vachata P, Hejcl A, Zolal A, Sames M. Validity of primary motor area localization with fMRI versus electric cortical stimulation: a comparative study. Acta Neurochir (Wien). 2009 Sep;151(9):1071-80. IF 1,472 (2009)

Impact factor of all publications: 11.433